SANDIA REPORT

Fractal-Like Materials Design with Optimized Radiative Properties for High-Efficiency Solar Energy Conversion

Clifford K. Ho, Jesus D. Ortega, Joshua M. Christian, Julius E. Yellowhair, Daniel Ray, John Kelton, Gregory Peacock, Charles Andraka, and Subhash Shinde (PM)

Sandia National Laboratories

Fractal-Like Materials Design with Optimized Radiative Properties for High-Efficiency Solar Energy Conversion

Clifford K. Ho, Jesus D. Ortega, Joshua M. Christian, Julius E. Yellowhair, Daniel Ray, John Kelton, Gregory Peacock, Charles Andraka, and Subhash Shinde (PM)

Concentrating Solar Technologies Department
Sandia National Laboratories
Albuquerque, NM 87185
(505) 844-2384, ckho@sandia.gov

Abstract

Novel designs to increase light trapping and thermal efficiency of concentrating solar receivers at multiple length scales have been conceived, designed, and tested. The fractal-like geometries and features are introduced at both macro (meters) and meso (millimeters to centimeters) scales. Advantages include increased solar absorptance, reduced thermal emittance, and increased thermal efficiency. Radial and linear structures at the meso (tube shape and geometry) and macro (total receiver geometry and configuration) scales redirect reflected solar radiation toward the interior of the receiver for increased absorptance. Hotter regions within the interior of the receiver can reduce thermal emittance due to reduced local view factors to the environment, and higher concentration ratios can be employed with similar surface irradiances to reduce the effective optical aperture, footprint, and thermal losses. Coupled optical/fluid/thermal models have been developed to evaluate the performance of these designs relative to conventional designs. Modeling results showed that fractal-like structures and geometries can increase the effective solar absorptance by 5 – 20% and the thermal efficiency by several percentage points at both the meso and macro scales, depending on factors such as intrinsic absorptance. Meso-scale prototypes were fabricated using additive manufacturing techniques, and a macro-scale bladed receiver design was fabricated using Inconel 625 tubes. On-sun tests were performed using the solar furnace and solar tower at the National Solar Thermal Test facility. The test results demonstrated enhanced solar absorptance and thermal efficiency of the fractal-like designs.

ACKNOWLEDGMENTS

CONTENTS

FIGURES

TABLES

8

1   INTRODUCTION

Conventional concentrating solar power receivers consist of panels of tubes arranged in a cylindrical or cubical shape, but these configurations also maximize radiative and convective heat losses to the environment; sunlight reflected off of these surfaces is lost to the environment. To increase the receiver thermal efficiency, previous research has focused on the development of solar selective coatings that increase solar absorptivity and reduce thermal emissivity. However, most of these coatings have been shown to suffer from degradation that reduces the lifetime performance of the plant and increases costs associated with reapplication [1]. In this work, we develop fractal-like receiver designs employing light-trapping structures and geometries at multiple length scales to increase the effective solar absorptance and efficiency of high-temperature receivers without the need for coatings.

Several previous researchers have looked at novel features or geometries to increase light trapping. Garbrecht et al. [2] evaluated pyramid shape receiver structures for molten salt power tower use. The pyramid structures extended from the base of the receiver, and the peaks faced the incoming solar radiation. It was shown that reflected losses could be reduced by 1.3% and thermal emission losses were reduced by 2.8%. The difficulty with these structures was achieving fluid flow within the peaks of the pyramids, and very hot spots developed at these locations. Another recent work considering fin structures within a parabolic trough receiver envelope was developed by Kasperski, et. al. [3]. This work showed that fin structures within the envelop cavity could increase efficiency by 13%. The National Renewable Energy Laboratory developed a super-critical CO_2 receiver design that takes advantage of alternative receiver geometries to increase light trapping and efficiency. They showed that a 92% efficiency can be achieved with a horizontal bladed receiver design [4], which is also described by a Sandia patent application [5]. While these previous studies evaluated features and geometries at a single scale, the current work looks to develop novel features and geometries across multiple length scales to further increase light trapping and thermal efficiencies.

Examples of fractal-like receiver designs employing light-trapping structures and geometries at multiple length scales are shown in Figure 1. Radial and linear structures at the meso scale (tube shape and geometry) and macro scale (total receiver geometry and configuration) redirect reflected solar radiation toward the interior of the receiver for increased light trapping and absorptance, which is in contrast to cylindrical and cubical shapes that reflect any incoming light back to the environment. Light-trapping features and texturing can also be applied at the micro scale (i.e., on the surface of the meso-scale tubes). A great deal of research already exists with the aim of developing high-temperature coatings, but this work focuses on fractal-like geometries at the meso and macro scales to achieve high efficiencies without the need for coatings. These fractal-like receivers can utilize conventional heat transfer fluids (e.g., molten salt and steam) used in CSP plants, but can also utilize super-critical CO_2 for increased power block efficiency, depending on specific designs and resulting allowable stresses. Structural analyses have been performed on these geometries for various pressure loads and thermal gradients to determine acceptable designs for prescribed operating conditions.

~10 m   meters   mm - cm

©SolarReserve

Conventional cylindrical
solar receiver

New fractal-like designs with increased light-
trapping features at multiple length scales
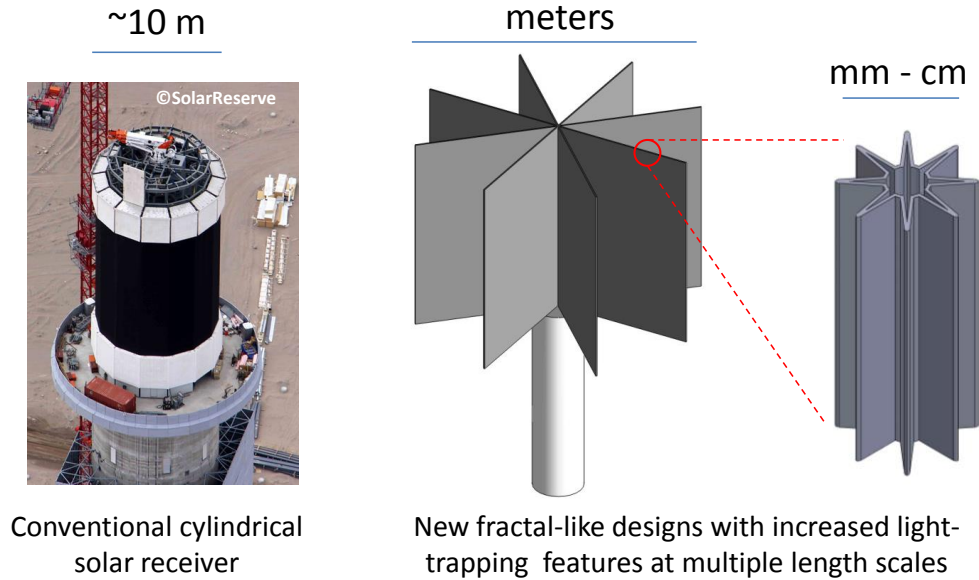
Figure 1. Conventional design (left) and examples of fractal-like designs and structures for solar thermal receivers to enhance solar absorptance at multiple length scales (patents pending [5, 6]).

Different designs for these light-trapping structures and geometries are shown in Figure 2. The macro-scale fractal-like receiver designs can accommodate both surround and directional (e.g., south-facing) heliostat fields. The designs can incorporate hat-like features to reduce radiative and convective losses from the top of the receiver, and the linear patterns can be oriented either vertically or horizontally. The linear panels (bottom left image in Figure 2) can also be placed side-by-side in a cylindrical pattern to accommodate a surround heliostat field. The meso-scale, fluid-carrying tubes employ similar features and geometries to trap the light and increase solar absorptance as shown in Figure 2. The tubes can be placed side-by-side or in various configurations to form the panels of tubes shown in the macro-scale designs. Additive manufacturing methods such as 3D printing, laser engineered net shaping, and powder bed fusion techniques can be used to fabricate the meso-scale tube structures. Filleted or rounded structures may be needed to reduce stress from thermal gradients and/or high internal fluid pressures. Optimization of these designs based on optical/thermal/fluid/structural analyses can be performed for full receiver panels composed of these alternative tube geometries.

The three technical objectives of this work were as follows:

1. Increase the light trapping and effective solar absorptance of the receiver by adding light-trapping features at multiple scales
2. Reduce the thermal emittance of the receiver by reducing the local radiative view factors in the hottest regions (e.g., interior) of the receiver
3. Increase the thermal efficiency and reduce heat loss of the receiver by increasing the concentration ratio and reducing the overall aperture size (optical intercept) while maintaining the same exposed surface area and average irradiance on the receiver surface

Macro (~0.1 – 10 m)   Meso (~0.1 – 100 mm)
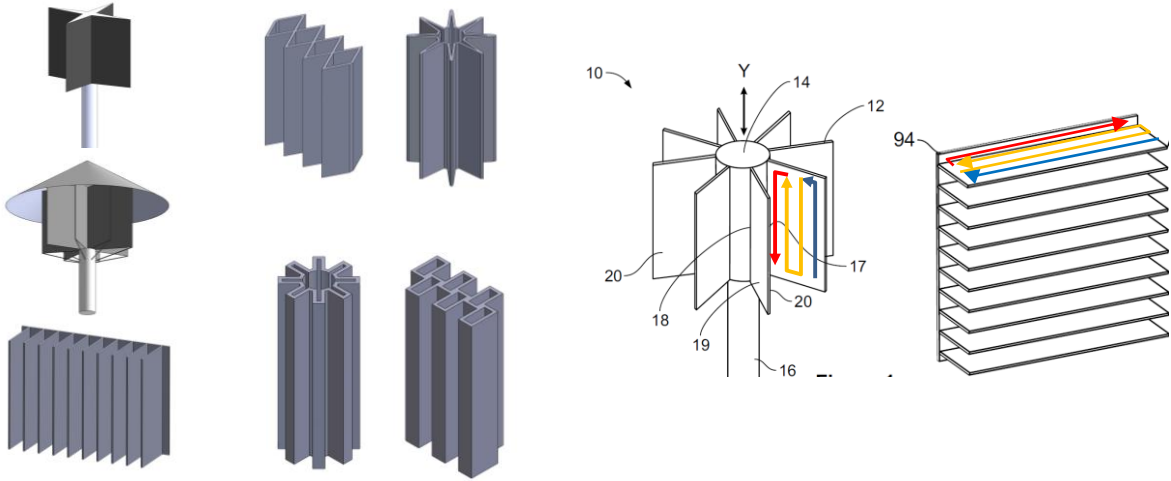
Figure 2. Left: examples of fractal-like receiver designs at the macro and meso scales. Right: direction of fluid flow in macro-scale designs (patents pending [5, 6]).

2   MODELING

2.1   Optical Modeling

The concentrated solar radiation incident upon the receiver can be modeled using ray tracing, cone optics, or other analytical methods [7]. Yellowhair et al. [7] concluded that ray tracing was most suitable for modeling complex receiver geometries such as those presented in this paper. The code SolTrace [8], a free ray-tracing tool customized for optical modeling of concentrating solar power systems, was benchmarked against other optical tools [7] and selected for use in this study.

Figure 3 shows a screen image of the receiver irradiance from a field of heliostats at Sandia's National Solar Thermal Test Facility. This example shows a radial STAR receiver geometry with simulated irradiance patterns on each side of the irradiated panels. A postprocessor was written in Matlab to import flux patterns from SolTrace into a file that could be read and applied as boundary conditions by ANSYS Fluent, a computational fluid dynamics software that can simulate thermal losses by radiative emittance and convection, heat absorption, and temperature distributions (Figure 4). Other analytical tools built into ANSYS Fluent (discrete ordinates radiation model) and Solidworks Flow Simulation were also used for thermal/fluid modeling. The use of these coupled optical/thermal/fluid models is advantageous when modeling complex geometries with large spatial scales. Additional details of the optical modeling tools can be found in Yellowhair et al. [9].
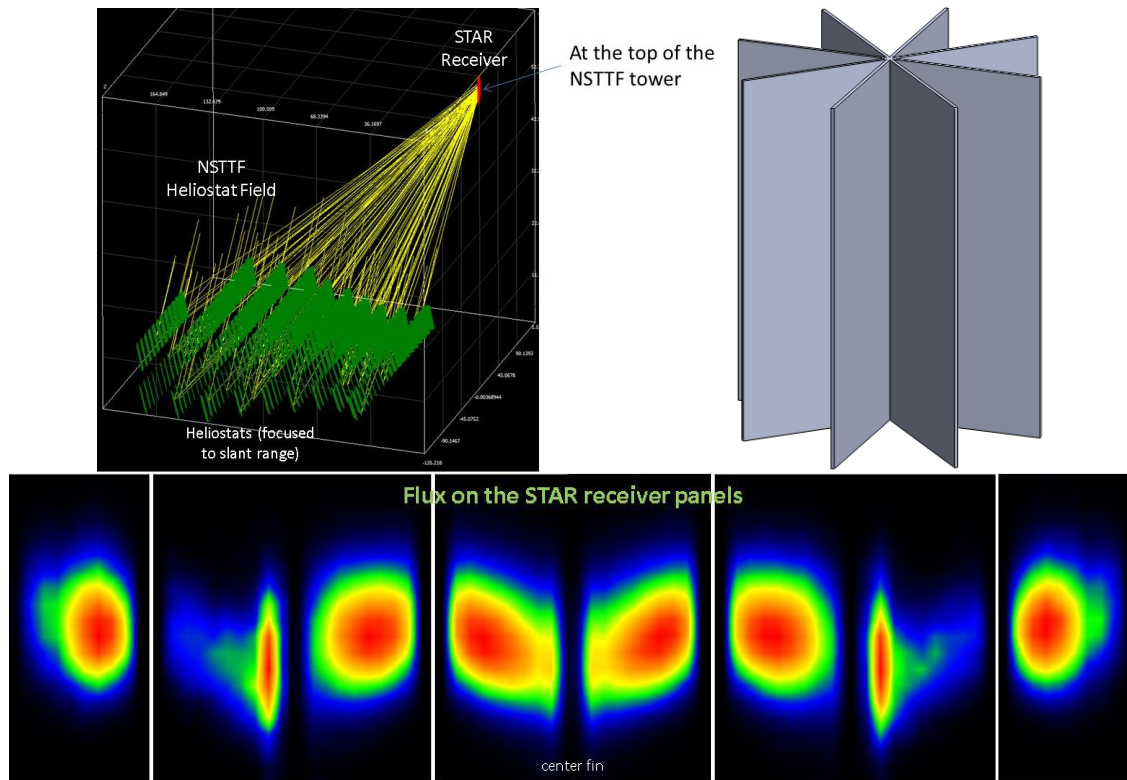
Figure 3. Optical modeling of irradiance from a field of heliostats on a STAR receiver geometry with radial panels.
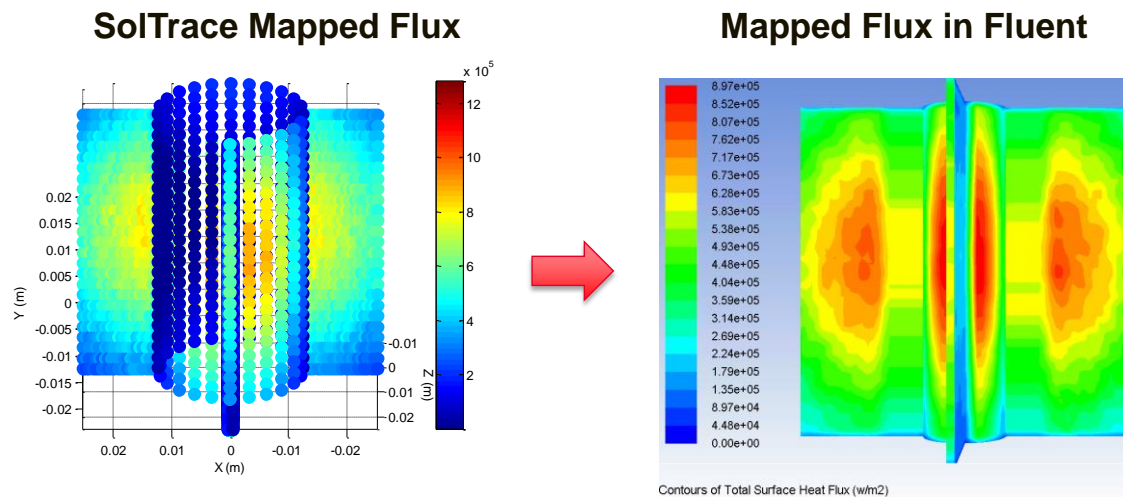
Figure 4. A post-processor was written in Matlab to transfer the irradiance from SolTrace into ANSYS Fluent as a heat flux boundary condition for CFD simulations.

2.2   Meso-Scale Modeling

Flat and vertically finned meso-scale structures were modeled to evaluate the potential enhancement of solar absorptance by surface features and structures. These meso-scale designs are intended to represent sections of non-conventional pipe geometries that can be used to carry the heat-transfer fluid while increasing the effective solar absorptance of the pipes with light-trapping structures at the meso-scale. Each piece is hollow with a wall thickness of 1 mm. The thermal properties of the substrate were assumed to be those of stainless steel 316 while the radiative surface properties are varied (e.g., solar absorptance varied from $0.5 - 0.95$ assuming a gray surface). A solar irradiance of 100 W/cm^2 (~1000 suns) was directed toward one side of each sample while the interior walls of each sample were maintained at 500 °C (average receiver temperature) to simulate a heat sink caused by the heat-transfer fluid. Half symmetry was employed so that only the right half of the samples were simulated. A grid convergence was performed, and over 1 million cells were used in each simulation. Radiation (solar and thermal), natural convection, and conduction through the walls were included in the models. The radiation model employs the discrete transfer (ray-tracing) method and assumes diffuse, gray-body radiation between surfaces.

Results show that while the finned geometry increased the amount of convective and thermal radiative heat loss due to the larger surface area, the solar reflected loss was significantly lower $(30 - 40\%)$, resulting in a lower total heat loss $(7 - 26\%)$. In addition, at lower material absorptances, the reduction in total heat loss was more pronounced. At higher material absorptances, the reduction in total heat loss was less. This indicates that if a receiver coating can maintain a high solar absorptance (~0.95), the use of flat or conventional shapes may be suitable. However, if the coating degrades below ~90% solar absorptance, the proposed fractal-like structures can increase the effective solar absorptance significantly. Figure 5 shows the thermal efficiency (net absorbed power divided by the incident power) and the increase in effective absorptance (absorbed solar power (neglecting convective and thermal radiative losses) divided by the incident power), which reflects this trend as a function of prescribed material absorptance. At a material solar absorptance of 0.95, the thermal efficiency of the flat and finned geometries are nearly the same, but if the material solar absorptance decreases to 0.9, the finned structure can increase the thermal efficiency by several percent. At a material solar absorptance of 0.7, the finned structure increases the thermal efficiency by 13%. Therefore, employing fractal-like designs and structures using plain substrate materials may be suitable in some cases without the need for coatings.
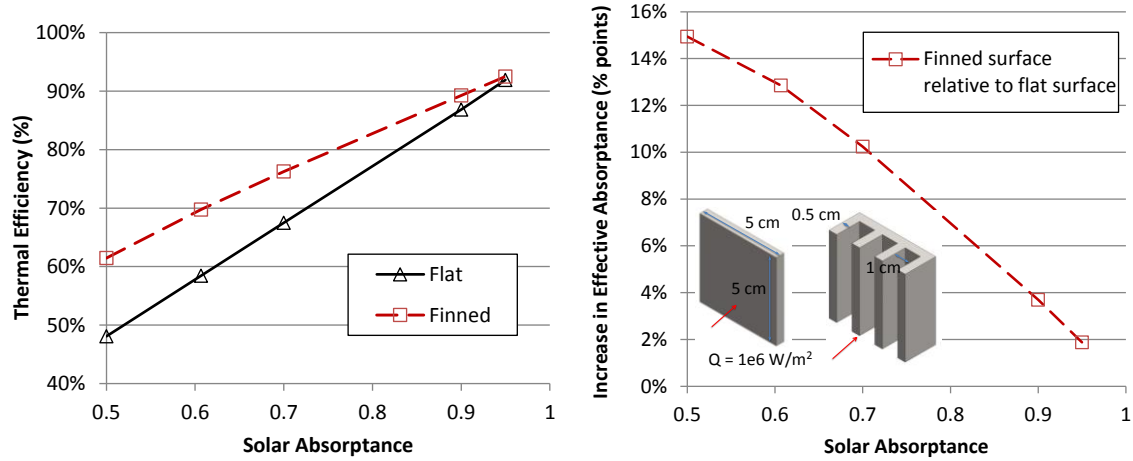
Figure 5. Simulated efficiency and increase in effective absorptance as a function of intrinsic material solar absorptance for flat and finned meso-scale geometries [10].

Simulations of different offsets and orientations of tubular geometries revealed that the effective solar absorptivity increased as the offset angle increased for circular, square, and rectangular tubes due to increased light trapping (Figure 6). For the diamond geometry, the effective solar absorptivity decreased as the offset angle increased. Simulations of different orientations of the tubular geometries showed that the effective solar absorptance can either increase or decrease as a function of orientation based on the available irradiated area and reflective losses (less light trapping).
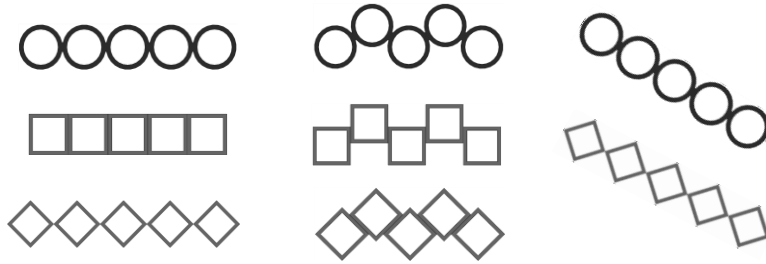
Figure 6. Examples of different meso-scale geometries, offsets, and orientations that were simulated.

ANSYS Mechanical was used to evaluate stress distributions within the tubes under expected thermal and mechanical loads. As expected, the stress levels at the corners of the rectangular and diamond tubes were higher than the circular tubes and exceeded allowable stress levels for high-pressure supercritical carbon dioxide operating conditions (20 MPa, 700 °C). An evaluation of the allowable stresses for molten-salt and supercritical carbon dioxide working fluids was summarized in Ortega et al. [11]. Rounded corners and increased tube thickness reduced the stress levels. Optimization of the tubular designs that satisfy both optical and structural requirements was performed.

Additional details of optical, fluid, thermal, and structural modeling can be found in Ortega et al. [12, 13] and are presented in subsequent sections describing the meso-scale testing.

2.3 Macro-Scale Modeling

2.3.1 Previous Work

Computational fluid dynamics (CFD) models were created to model the macro-scale designs of solar receivers employing light-trapping features and geometries. Early work developed models to replicate the Solar Two receiver and to verify experimental results seen at the pilot plant. Christian et al. [14] verified that CFD can be used to evaluate thermal losses from an external receiver when compared to experimental results. This information has led to confidence in using CFD to look at alternative receiver designs and evaluate how they should perform under some operating conditions.

Initial work at SNL for alternative receiver designs focused on comparing different receiver geometries to the base case study of a cylindrical receiver design (Solar Two) (see Figure 7 for alternative receiver designs). Note that the receiver base case changed within this study to a flat plate geometry due to the anticipated experimental efforts at the NSTTF. CFD analysis was performed on several different receiver geometries to determine impacts on thermal efficiencies. These receiver designs had the same exposed surface area and a constant temperature applied to the surface while evaluating radiation, natural convection, and forced convection (wind speed of 7 m/s). The constant temperature condition was a first-cut, quick modeling effort to understand if receiver geometries could impact efficiency significantly. Results presented in [15] detail the initial work that shows a thermal efficiency increase of close to 10% is possible with these alternative designs (see Figure 8).
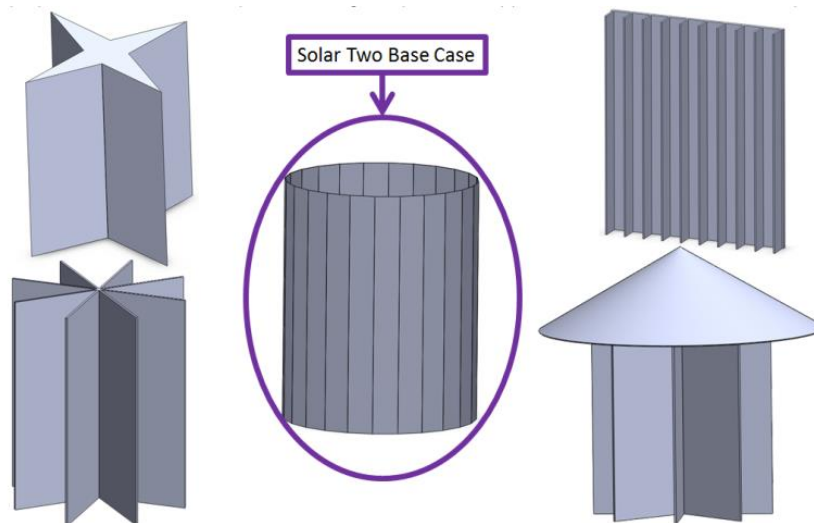
Figure 7. Initial receiver design concepts for comparison to a base-case cylindrical receiver [16]

16

$$\eta = 1 - \frac{Q_{loss}}{Q_{in}}$$

$$Q_{in} = Q_{loss} + Q_{absorbed}$$

- $Q_{absorbed}$ is assumed to be 35.77 MW for all cases
  - 35.77 MW taken from Solar Two analysis performed by Christian et al.[1]
- Q_{loss} is found from FLUENT simulations
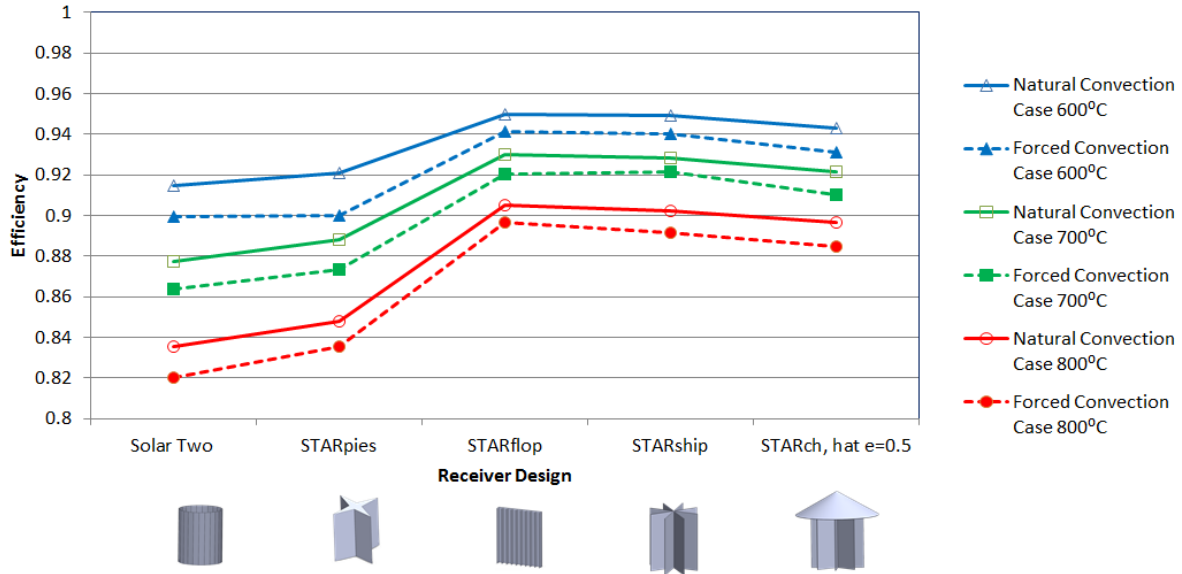
Figure 8. Receiver thermal efficiencies with three different temperature inputs and evaluating natural and forced convection effects [15].
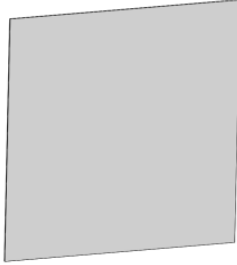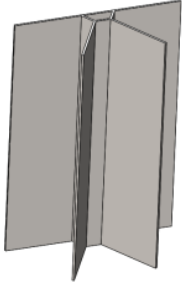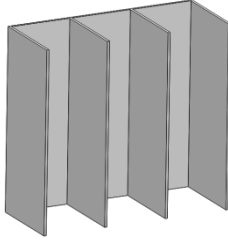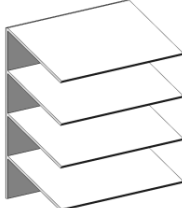
The work in [15] concluded that varying receiver geometric designs can impact thermal efficiency of a receiver. The current work of this project is meant to fully validate the advantages of new receiver designs. The receiver geometries changed for the following work based on possible experimental work. The new receiver designs were designed such that they would be easier to fabricate and test at the NSTTF (north-facing receivers). The new receiver geometries can be seen in Table 1. Each of these designs are meant to achieve three technical objectives.

The three technical objectives (TO) that served as a guideline for developing the new receiver for testing were:

1. Increase the light trapping and effective solar absorptance of the receiver by adding radial or linear structures

2. Reduce the thermal emittance of the receiver by taking advantage of local view factors in the hottest regions of the receiver

3. Increase the thermal efficiency of the receiver by increasing concentration ratio of the receiver through the use of a smaller overall aperture size (optical intercept) while maintaining the same exposed surface area and power

Spillage is currently not considered for this work. The focus is to first identify if it is possible for these different receiver geometries to achieve higher thermal efficiencies.

Table 1. Macro-scale receiver designs [16]

Base Case Study-Billboard; Height = 2 m; Width = 2 m; Exposed Surface Area = 4m^2	
Radial Finned Receiver; Height = 1.5 m; Width = 1 m; Exposed Surface Area = 4m^2; Fin length = 0.4 m	
Linear Vertical Fin Receiver; Height = 0.95 m; Width = 1 m; Exposed Surface Area = 4m^2; Fin length = 0.4 m	
Bladed Receiver; Height = 0.84 m; Width = 1 m; Exposed Surface Area = 4m^2; Fin length = 0.4 m	

Technical objective 3 has been evaluated with CFD models to understand the impact of fin arrangement based on re-radiation from surface to surface by Christian et al. [17]. The results during this preliminary analysis showed that the Bladed Receiver performed best, using thermal efficiency as the primary metric. Figure 9 shows part of the results from Christian et al. [17] showing a single aim point ray trace and thermal analysis of the receiver designs.
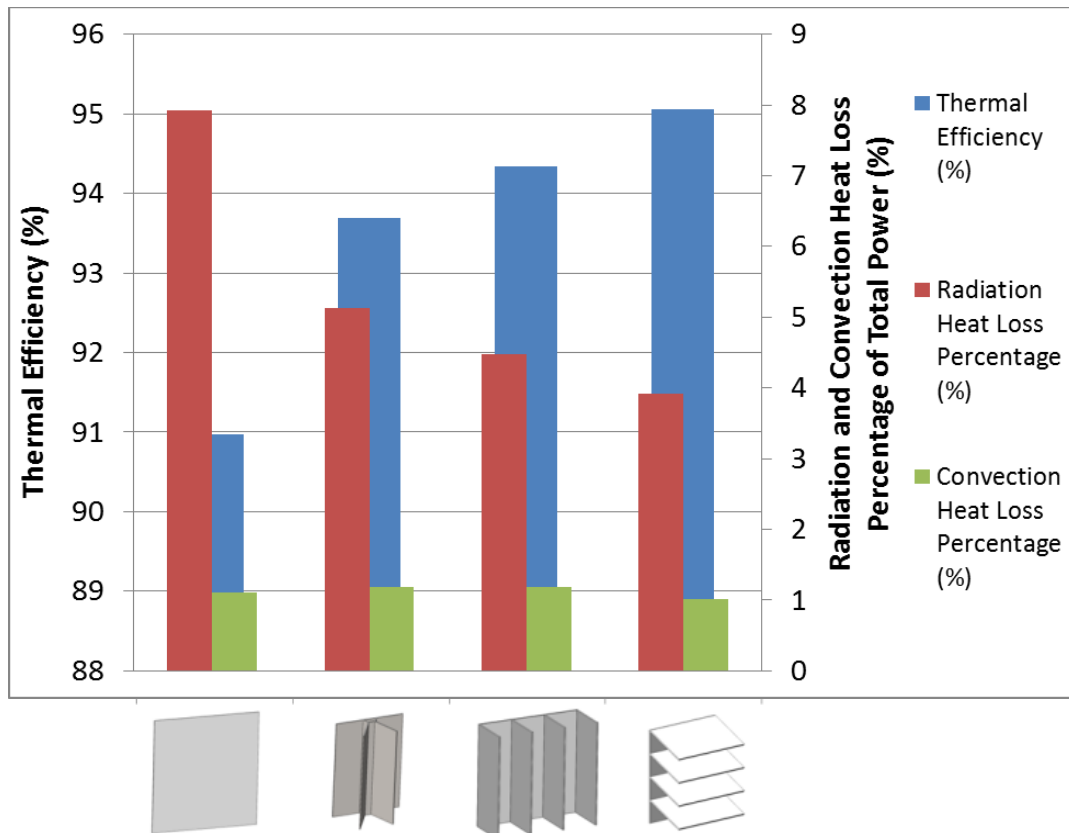
Figure 9.. Thermal efficiency and heat losses for alternative macro-scale receiver geometries with an average irradiance of 500 kW/m^2 [18].
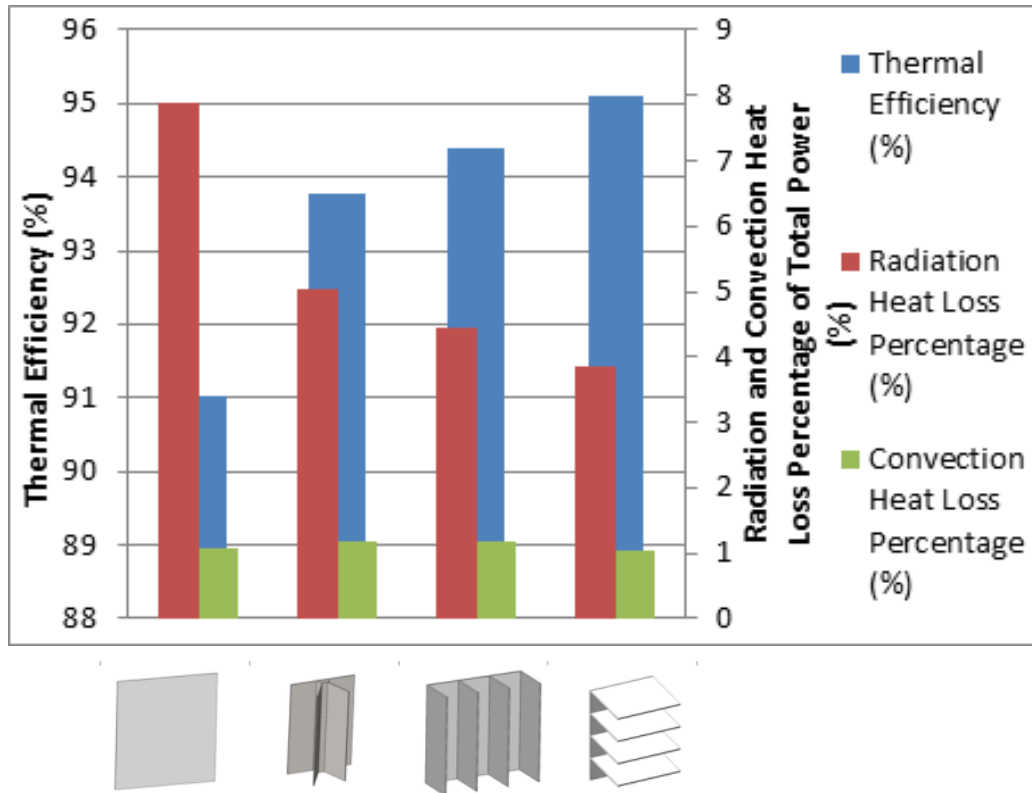
Single aim point ray traces thermal efficiency, radiation heat loss percentage of total heat input, and convection heat loss percentage of total heat input for the different receiver geometries

2.3.2 Receiver Geometry Evaluation

The process evaluated the four receivers utilizing ray tracing to determine the effective absorptance of the designs. From this point, a single receiver design with the most promising results was pursued. This receiver design was subjected to more rigorous ray tracing optimization analysis, CFD, and structural analysis for experimentally comparing this receiver to a base-case flat panel receiver at the National Solar Thermal Test Facility (NSTTF) at Sandia National Laboratories. Due to time and resource constraints, only a single alternative receiver design could be pursued.

Soltrace is a free ray tracing code developed by the National Renewable Energy Laboratory (NREL) and utilized extensively for this analysis. It is specially written to address CSP modeling needs. It was used to evaluate the optical performance of the receiver designs initially proposed and reported in Christian et al. [17]. Each receiver was imported into Soltrace and evaluated for effective solar absorptance based on initial incident radiation from the heliostat field and any re-reflections from any surface to another surface. The final receiver design was then chosen based on the ray-tracing results and previous CFD analysis. The final design was then subjected to a parametric analysis evaluating the number of fins, length of fin, and angle of fin to determine which receiver modification should be fabricated and tested.

The four receivers in Table 1 had a ray trace performed using the NSTTF heliostat field. The heliostat field remained constant through each study. The heliostat facets were 96% reflective with a slope error of 1 mrad, and the receiver surface reflectivity was varied between 0, 0.04, and 0.14 in order to get an effective absorptivity of the receiver. Two overall cases were evaluated using a single aim point versus a four aim point model.

Each receiver was evaluated using effective absorptivity as the final design metric. The greater the effective absorptance translates into a better performing receiver due to the light trapping effect. The effective absorptivity is defined as:

$$Effective\ Absorptivity = \frac{Absorbed\ Power, Surface\ Emissivity\ less\ than\ 1}{Absorbed\ Power,\ Surface\ Emissivity\ of\ 1}$$

Table 2. Soltrace effective absorptivity for different surface emissivities

Geometry	Surface Emissivity	Single Aim Point Effective Absorptivity	Four Aim Points Effective Absorptivity
	0.86	0.86	0.86
	0.96	0.96	0.96
	1	1	1
	0.86	0.94	0.93
	0.96	0.98	0.98
	1	1	1
	0.86	0.94	0.93
	0.96	0.98	0.98
	1	1	1
	0.86	0.96	0.96
	0.96	0.99	0.99
	1	1	1

The results of this ray trace analysis show that the effective emissivity of the Bladed Receiver can reach up to 0.96 when the surface emissivity is 0.86 which corresponds to a receiver surface with no selective absorber coating. The advantage of this light-trapping effect is that a selective absorber coating would no longer be required if the effective absorptivity can match the performance of a coated surface. Ho et al. [19] measured Pyromark 2500 to produce an absorptance of 0.96-0.97 for temperatures up to 600°C which is on par with the results seen for the Bladed Receiver.

The results of this ray trace analysis and the CFD for these same receiver designs showed that the Bladed Receiver had the highest thermal (~95%) and optical performance (effective absorptivity = 0.96). This design was chosen for prototype development due to the ability to just test one receiver design for validation. The following results evaluate an optimized receiver design through ray tracing, CFD, and structural analysis for prototype testing at the NSTTF.

2.3.3 Ray Tracing for Bladed Receiver

The Bladed or bladed receiver has many options in terms of number of fins, number of tubes, and the angle of the fins (with respect to the vertical). In order to provide semi- optimized receiver geometries for the thermal performance analysis, an algorithm was developed to determine receiver dimensions for a parametric ray-trace analysis (detailed by Equation 1). The receiver image in Figure 10 shows the dimensions that were varied to determine the most optically efficient receiver design with a fixed incident power across all cases with the aim point(s) focused on the back wall of the receiver. The h dimension is defined by the number of tubes for the back wall sections times the tube diameter. The t dimension is driven by the number of tubes in the fin panels times the tube diameter. The tube diameter is always constant.
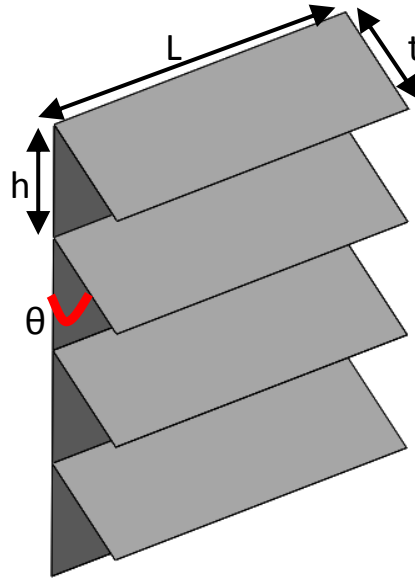
Figure 10. Semi-optimization of horizontal receiver dimensions for ray-trace optical efficiency analysis.

$$n_t = \frac{A}{2D^2 N^2 (n_h + 1)} - \frac{n_h}{2}$$

Where n_t is the number of tubes on a single fin panel, n_h is the number of tubes on a back wall panel, N is the number of fin panels, A is the overall surface area of the receiver (not including the back side), D is the tube diameter. The parametric cases are developed by varying n_h and N to determine the required n_t. N was varied between 3, 4, and 5 while n_h was varied between 5 to 15 with a step of 1. This set of receiver geometries were then subjected to a varying θ which is the angle between the fin panel and back wall. θ was varied between 20° to 60° with a step size of 5°. The three variables resulted in 297 case studies. Each study was then imported into SolTrace where an incident power, of similar magnitudes, from the NSTTF heliostat field was applied to each geometry. Figure 11 shows the flux profile on a flat plane, which is representative of the back wall on the receiver. The flux profile was created with a single aim point at the center of the receiver and using 20 heliostats to produce 0.5 MWt on the receivers.
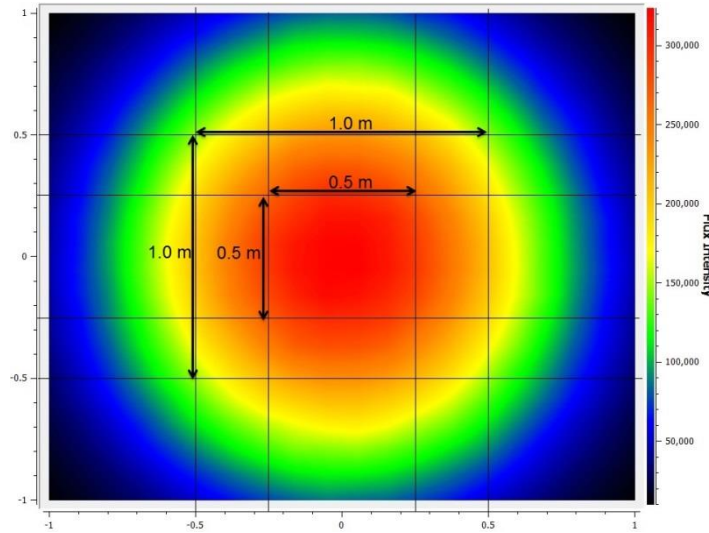
Figure 11. Single aim point, 0.5 mwt on a 2 m x 2 m aperture used for all ray-trace studies to compare optical efficiency of parametric receivers.

Each case was then evaluated for an effective absorptance based on the absorbed power on the receiver divided by the incident power on the receiver. The cases evaluated thus far that have shown an effective solar absorptance of 96.5% or higher are described in Table 3 with plotted results shown in Figure 12. The error bars on represent a 0.5% variation in the ray trace results due to the random ray generation within SolTrace.

A down-selection process has been performed to pick a receiver, based on the ray-trace analysis, for the experimental validation. The chosen receiver design is highlighted in Table 3 and is case 75. Case 75 has a θ value of 50°, three fins (N=3), 13 tubes on the back panel (n_h=13), and 18 tubes on each fin (n_t=18). Case 75 was chosen over other cases with similar absorptance values

based on the heat flux distribution seen on the surfaces compared to the other cases. Figure 13 displays the heat flux distribution on case 75. The ray-trace predicts that the hottest flux regions will be on the lower half of the back panels and on the tips of the fins. The tips of the fins are planned to be "dummy" tubes made of ceramic to avoid failure at these tips. The heat flux on the fins is fairly uniform across the fin surfaces making this receiver an ideal candidate. Another selection criterion for this case number was the actual number of fins. Three fins are easier to fabricate and test in prototype scale making it an ideal candidate over the four or five fin cases.

Table 3. case descriptions with effective solar absorptance of greater than 90%.

Case	θ	N	n_h	n_t	Effective Solar Absorptance
64	45	3	13	18	96.5%
74	50	3	12	20	96.6%
75	50	3	13	18	96.6%
85	55	3	12	20	96.7%
86	55	3	13	18	96.5%
94	60	3	10	26	96.6%
95	60	3	11	23	96.8%
138	35	4	10	13	96.6%
148	40	4	9	15	96.6%
159	45	4	9	15	97.0%
160	45	4	10	13	96.8%
169	50	4	8	18	96.6%
170	50	4	9	15	96.8%
171	50	4	10	13	97.0%
180	55	4	8	18	96.6%
181	55	4	9	15	97.0%
182	55	4	10	13	96.6%
191	60	4	8	18	96.9%
192	60	4	9	15	96.8%
234	35	5	7	12	96.6%
235	35	5	8	10	96.8%
245	40	5	7	12	97.0%
246	40	5	8	10	97.0%
256	45	5	7	12	97.1%
257	45	5	8	10	96.9%
266	50	5	6	15	96.6%
267	50	5	7	12	97.1%
268	50	5	8	10	96.9%
277	55	5	6	15	96.8%
278	55	5	7	12	97.0%
288	60	5	6	15	96.9%
289	60	5	7	12	96.9%
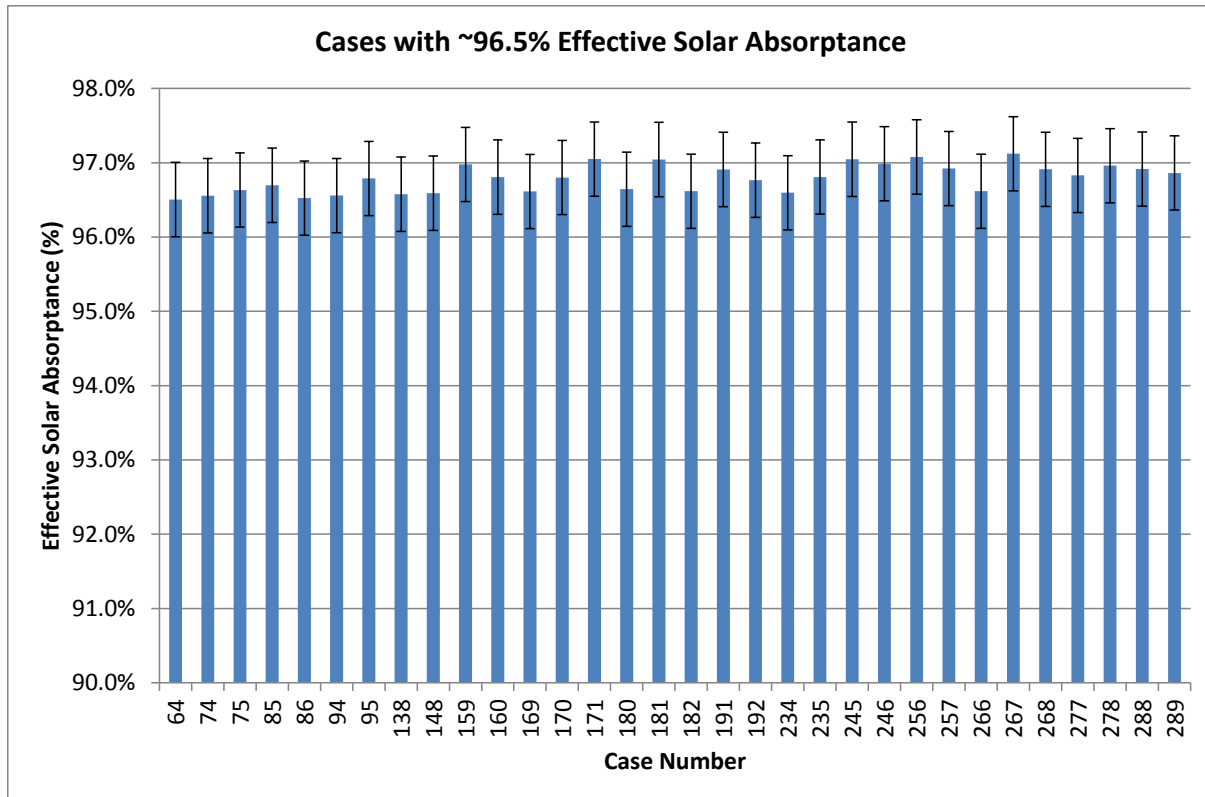
Figure 12. effective solar absorptance greater than 96.5% for the horizontal receiver.
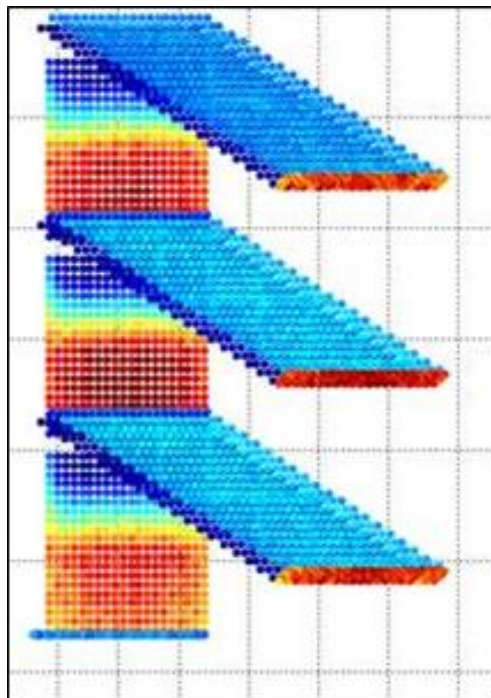
Figure 13. Heat flux distribution on case 75 with red being the hottest flux and dark blue being the lowest flux.

Computational Fluid Dynamics models were developed to evaluate the thermal performance of the Billboard and Bladed Receiver with the flux patterns evaluated during the ray-trace. A ray-trace to CFD code was written at SNL to integrate the results from SolTrace into the boundary conditions needed in ANSYS Fluent. The receiver will have a flux applied on the surface and have a HTF flowing through the panels. The thermal performance, measured by receiver thermal efficiency, is evaluated while changing flow patterns to take advantage of hot regions on the receiver with low local view factors (Technical Objective 2).

The receiver panels were modelled as cylindrical tubes stacked to form the entire panel. The billboard receiver has four panels composed of a total of 80 tubes with an aperture size of 1 m x 1 m. The Bladed Receiver design is based off the most promising receiver geometries evaluated in the ray-tracing. Several geometries were modelled for thermal performance. The billboard receiver and an example receiver for the Horizontal fin receiver are shown in Figure 14.
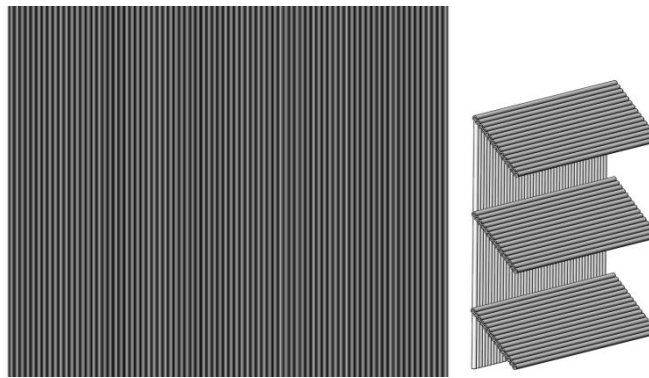
Figure 14. (left) Billboard receiver design (front view); (right) Bladed receiver example geometry (isometric view).

2.3.4 Structural Analysis

The overall structure of the receiver was comprised of cylindrical tubes that are stacked in order to achieve the panel structures needed to compose the fins and back walls of the receivers. The billboard design and Bladed Receiver have tubes welded into headers, similar to designs seen at both Solar One and Solar Two. An in-depth analysis was performed in previous work looking at the tube structural strength under pressure and temperature loading of the system [20]. The process for design included FEA which was validated against analytical models. The boundary conditions evaluated were:

- Pressures: 20 and 25 MPa

- Temperatures: 700°C and 650°C (corresponding to respective pressures above)

- Outer Diameter: 12.7 mm

- Tube wall thickness: 2.7686 mm

- Material: Haynes 230

27

It was shown that the chosen tube geometries could withstand the temperatures and pressures structurally, including creep and fatigue damage over the lifetime of the tube. The results of Ortega et al. [20] showed that according to the receiver needs, the structural analysis can be re-run with confidence under different loading or tube dimension conditions which was necessary in the case of the prototype receivers. The prototype receiver tube material was originally Haynes 230, but due to manufacturing time constraints Inconel 625 was used. The analysis was repeated using Inconel 625 to verify that the current tube dimensions and loading conditions could be withstood by the new material.

2.3.5 Summary of Macro-Scale Modeling

Four macro-scale fractal-like receiver configurations were modeled: flat (reference case), radial panels, horizontal louvered panels, and vertical panels [18]. The thermal efficiency, convective heat loss patterns, and air flow around each receiver design were simulated using ANSYS FLUENT. Simulated results of alternative macro-scale geometries showed that thermal efficiencies were increased by nearly 5% with radial or linear bladed receiver configurations. The horizontal louvered design was best, followed by the vertical and radial panel designs. Radiative losses were reduced with the fractal-like geometries due to reduced local radiative view factors in the hottest interior regions of the receiver. Convective losses were slightly higher in the vertical panel configurations, while convective heat losses were reduced in the horizontal louvered panel configuration. With the horizontal louvered configuration, convective heat losses from the hot interior regions of the receiver can be recuperated in cooler regions, thereby reducing the overall convective heat loss [21]. Additional modeling of the finalized horizontal bladed receiver design is provide in Section 3.2.

3   TESTING

3.1   Meso-Scale Testing

The solar furnace facility at Sandia's National Solar Thermal Test Facility (NSTTF) can provide 16 kW thermal power and up to 600 W/cm^2 peak irradiance over a 5 cm spot size. The solar furnace consists of a sun-tracking heliostat (95 m^2) which directs the sunlight towards a fixed dish concentrator (6.7 m diameter) housed in a building. The dish focal length is 4.1 m were the test articles are placed. Just outside the building between the heliostat and dish is a louver type attenuator system which controls the amount of light that is incident on the dish. The solar furnace facility is shown in Figure 15.

Meso-scale receiver parts with fractal-like geometries that were fabricated and tested are shown in Figure 16. The parts are 5 cm tall and were fabricated from Inconel 718 using the power-bed fusion technique. The flat plate was used as a baseline for comparison to the other geometries. Before exposing the flat part, its reflectance was measured with the Surface Optics 410-Solar reflectometer, which showed 24% reflectance (solar absorptance ~0.76). The reflectance was measured again after exposure and oxidation, which showed a reflectance of 14% (solar absorptance ~0.86). When the samples were pre-oxidized at 800 °C in an oven, the solar absorptance of oxidized Inconel 718 reached values greater than 0.9.

The receiver parts were placed, in pristine conditions (i.e., unoxidized), at the focus of the dish concentrator one part at a time. The variable attenuator was then opened to 5% and the parts were illuminated for up to two minutes until the surface temperature reached ~700°C as measured with an infrared camera. The 5% attenuator opening provided ~30 W/cm^2. Photographs of the receiver parts, using a digital camera, before and immediately after opening the attenuator and about a minute later were captured. The photographs were then analyzed with the PHLUX tool.[22]
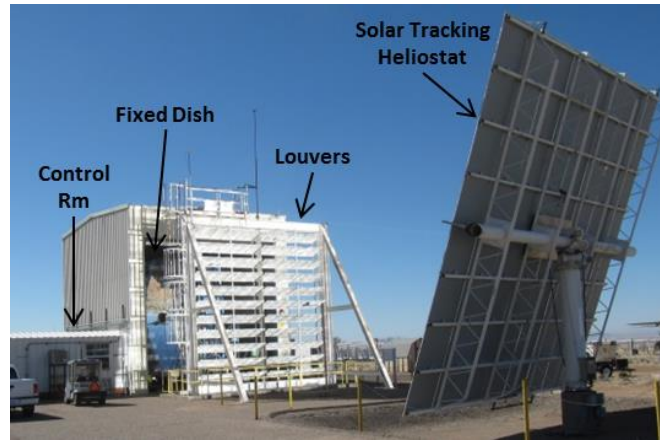
Figure 15. Solar furnace facility at the NSTTF that can provide 16 kW$_{th}$ and up to 600 W/cm^2 peak flux..

Flat Plate   0° Offset Tubes   30° Offset Tubes   45° Offset Tubes

Diamond Tubes   Offset Rectangles
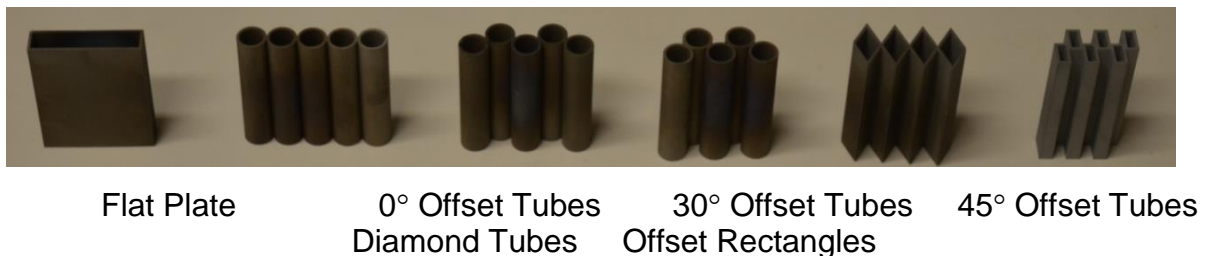
Figure 16. Prototype meso-scale fractal-like receiver parts fabricated with power-bed-fusion additive manufacturing using Inconel 718. The parts are all 5 cm tall and were tested on-sun in the solar furnace at ~30 W/cm^2.

Digital images were recorded and processed using the PHLUX method [22] to determine the relative irradiance distribution on each sample. These were then compared to ray-tracing simulations (Figure 17). Ray-tracing results show a similar irradiance patterns as the PHLUX processed images. The ray-tracing results show that absorptance is improved for the fractal-like geometries due to their light-trapping properties. The incident radiation was directed into the valleys of the corrugations, increasing solar absorption. The effective absorptance from each part was determined using SolTrace. The analysis was performed in two steps. The first step was to determine the total solar power incident on the receiver surfaces. This is single

incidences of the solar rays on the receiver surfaces after which the rays were terminated. In the second step, the incident solar rays were allowed to reflect off the receiver surfaces multiple times. On a flat surface, the rays reflect only once and the reflected rays are lost into the atmosphere. However, for the fractal-like receiver geometries, there can be multiple reflections between the surfaces and into corrugations causing a light-trapping effect. This leads to more absorption of the incident solar radiation by the receiver surfaces. The ratio of the total absorbed solar radiation and the total incident solar radiation were taken. The results for each receiver part are shown in Figure 18 for two different intrinsic material absorptances. Results show that relative to a flat plate, the new geometries could increase the effective solar absorptance from 86% to 92% for an intrinsic material absorptance of 86% (e.g., oxidized Inconel 718), and from 60% to 73% for an intrinsic material absorptance of 60% (e.g., alumina).

This significant finding shows that fractal-like receiver designs employing light-trapping structures and geometries at multiple length scales can increase the effective solar absorptance and efficiency of high temperature receivers without the need for selective absorber coatings or high-temperature paints.
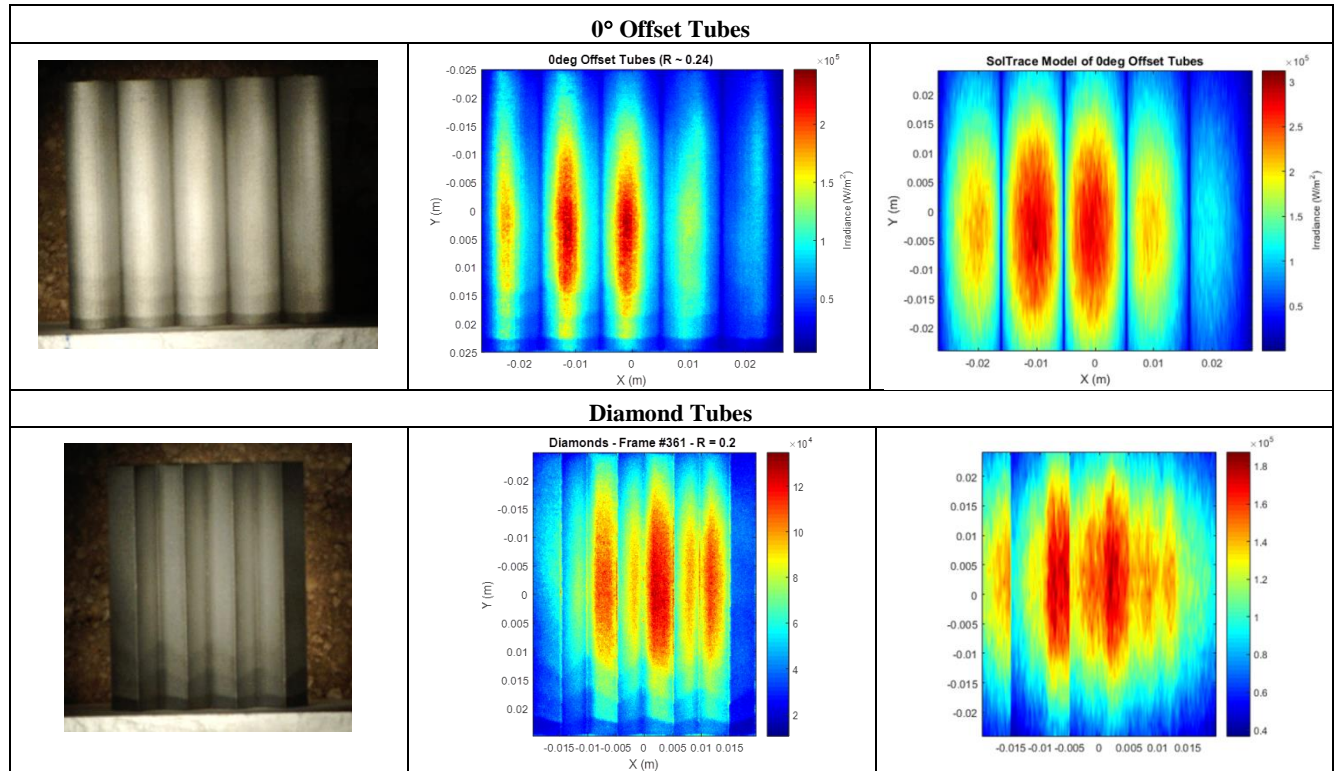
Figure 17. Test results showing photographs (left), irradiance measurements (middle), and model predictions (right) for two different tube configurations.
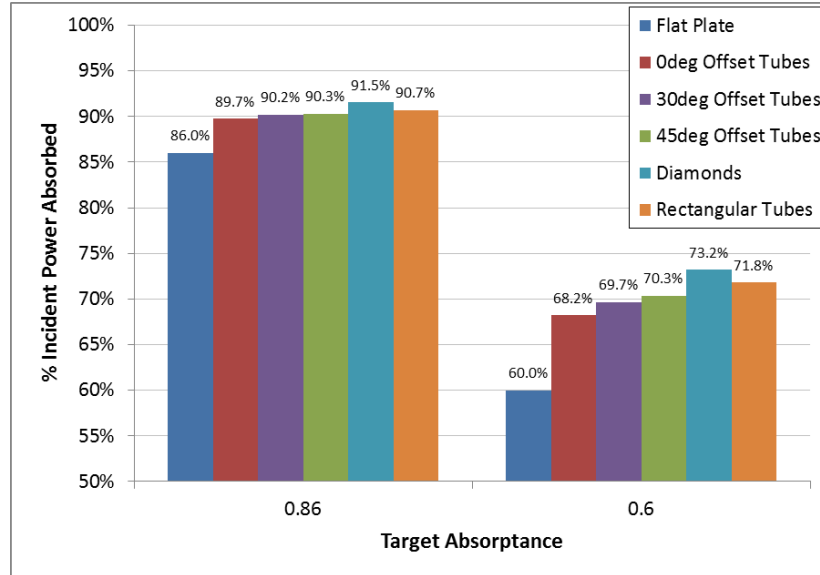
Figure 18. Results of the optical simulations showing absorptance improvements from the fractal-like receiver geometries relative to a flat plate receiver.

These results documented by Yellowhair et al. [6] were intended to demonstrate a potential increase in solar absorptivity by creating a light trapping effect in several types of geometries (Figure 2) by using patterns which could create multiple reflections. However, the increase in effective solar absorptance does not necessarily correlate with a potential increase in thermal efficiency. In the following sections, the thermal efficiency of the FLGs were investigated using calorimetric methods in the solar furnace.

In order to evaluate the thermal efficiency of the FLGs, two manifolds were added to the geometries which are connected to a test rig. The manifolds consist of a rectangular channels that are attached at the bottom and top of the part with inlet and outlet ports, respectively. These ports can be connected to the test rig by using a Swagelok fitting. These new parts were built out of Inconel 718 metal using the direct metal laser sintering (Figure 19). The samples were oxidized for 20 hours at 800°C in order to achieve the solar absorptivity required.
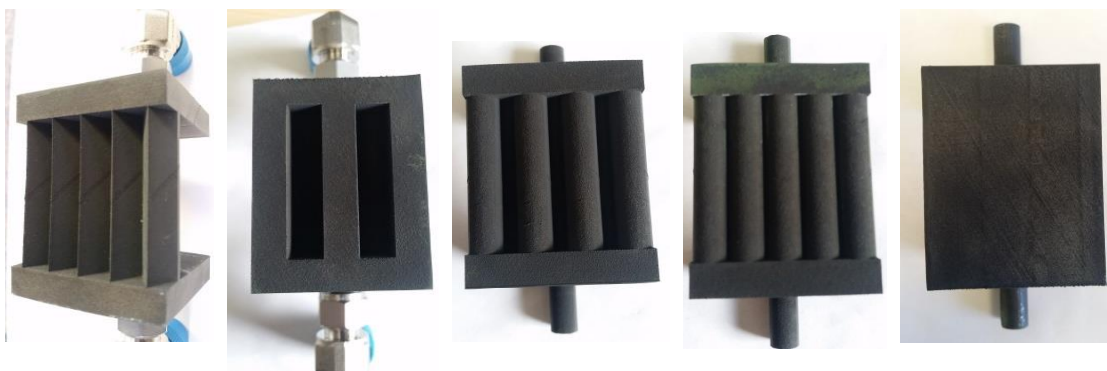
Figure 19. New FLGs with manifolds. From left to right: diamond channels, rectangular channels, 45° offset cylinder tubes, 0° offset cylinder tubes, and flat plate [5].

These FLGs have a frontal area of ~5 cm x 5 cm which matches the beam size from the solar furnace. The parts were built with a wall thickness of 1 mm to minimize the amount of material required for construction. The test loop is a calorimetric setup built to evaluate the thermal performance of the receivers. The complete test loop was composed by an air blower, a regulating valve, an air flow meter, and a thermocouple in the inlet and the outlet (Figure 20). The test loop was able to accommodate all the FLGs to be tested in the solar furnace.
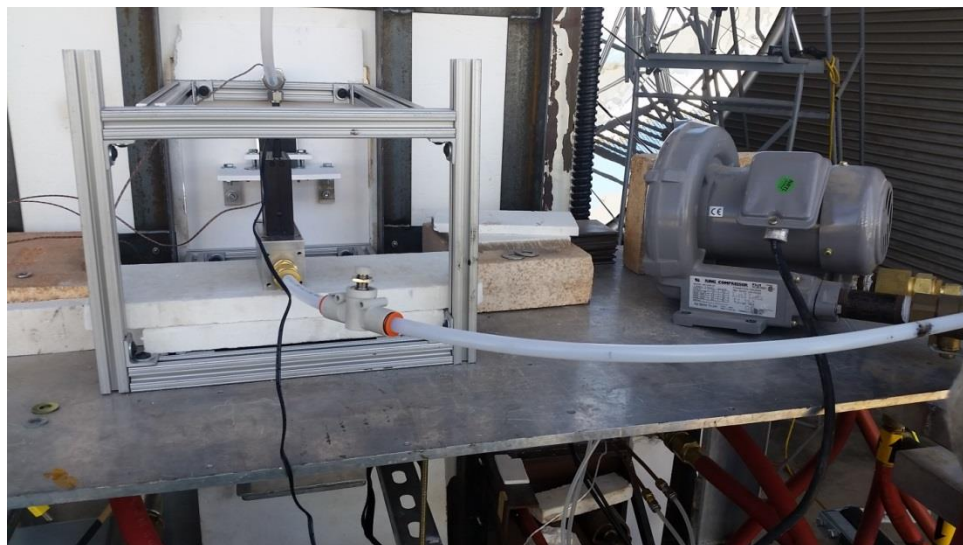
Figure 20. Complete test loop.

Spillage board was required to avoid flux spillage to the rest of the test loop components (Figure 21 and Figure 22). This also limited the irradiance that will intersect other regions of the part.
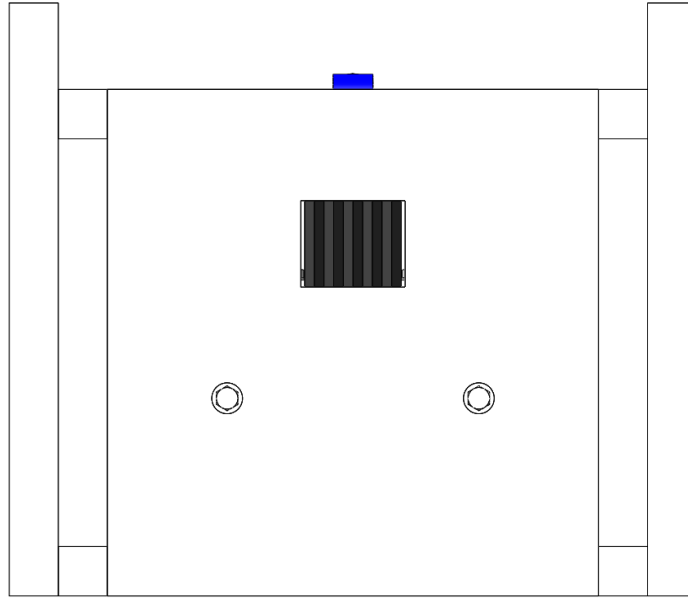
Figure 21. Spillage board located in the front of FLG mount. Aperture dimensions (W x L): 5 cm x 5.1 cm.
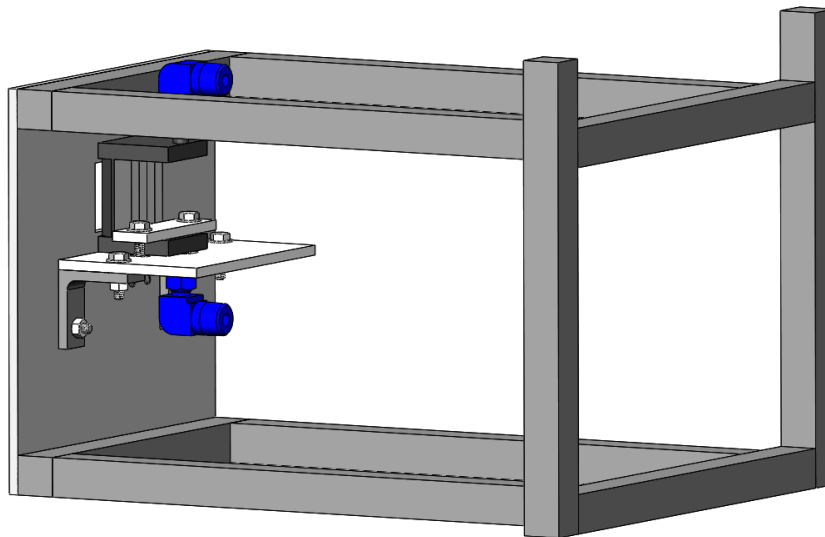
Figure 22. FLG complete mount. The part is located ~1.5 mm behind the 6.35 mm spillage board.

The solar furnace at the SNL National Solar Thermal Test Facility (NSTTF) is capable of providing 16 kW thermal power and up to 7000 W/cm^2 peak irradiance over a 5 cm beam size [6]. The FLGs were placed at the focus of the dish concentrator while the blower was running at 50 SLPM (i.e. Standard liters per minute). The attenuator was then opened enough to reach two concentration levels ~15 and 30 W/cm^2. The concentration levels were measured using a flux Kendall. The attenuator settings were in turn used to apply a heat flux on the FLGs. Inlet and outlet temperatures were recorded along with the flow rate and direct normal irradiance (DNI).

Photographs were taken during the tests and were analyzed with the PHLUX tool [8] as shown in Figure 23 and Figure 24.
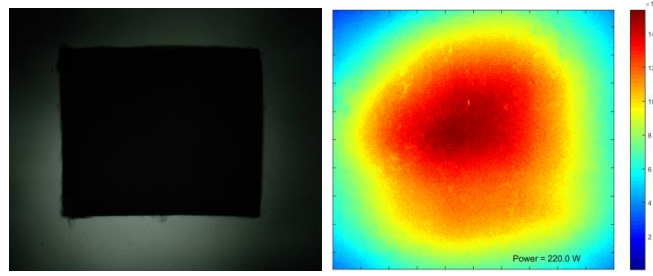
Figure 23. Left: Heat flux incident on the flat plate. Right: Heat flux applied on the FLGs ~15 W/cm^2.
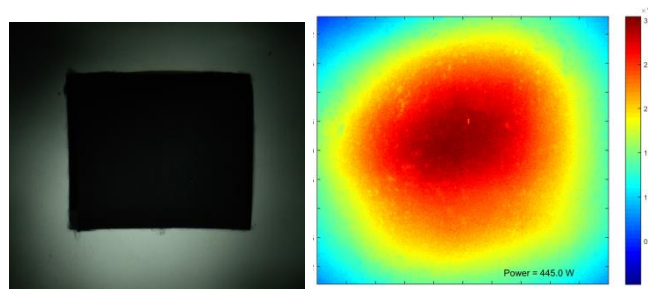
Figure 24. Left: Heat flux incident on the flat plate. Right: Heat flux applied on the FLGs ~30 W/cm^2.

The heat fluxes in Figure 23 and Figure 24 represent the heat flux distribution on a flat surface. The heat flux incident on this surface is the same used on the part. This heat flux is applied using the geometric center of the part as the aim-point.

After the tests were completed, the flow rate was reduced to ~35 SLPM and the outlet temperatures were targeted to match to those in the previous tests. The attenuator setting were adjusted in order to achieve equal outlet temperatures. These high and low equivalent fluxes varied between FLGs and they are presented in Table 4.

The peak surface temperatures were monitored using a laser thermometer. The peak surface temperature was used as a separate measure to build the computational models. Peak temperatures of ~1000°C were recorded due to the limited flow rates that the blower was able to provide.

The thermal efficiency is evaluated as shown in Eq. (1). Where $\dot{Q}_{abs}$ is the heat is absorbed by the air flow and $\dot{Q}_{in}$ is the heat incident on the part. The values of the heat incident on the part are based on the amount of heal flux that intersects the aperture over the size of the aperture.

$$\eta = \frac{\dot{Q}_{abs}}{\dot{Q}_{in}} \tag{1}$$

Table 4 shows the incident heat calculated for every case. The results (
Figure 25) show an increase in the thermal efficiency when compared to the flat plate in all
instances. The increase in thermal efficiency can be attributed to the light-trapping and by the
features of the FLGs.

Table 4. **The Incident power applied to the FLGs.**

	Flux Level (W/cm²)	Power on Aperture (W)	Flux Level (W/cm²)	Power on Aperture (W)
Diamond	15	229	13	184
	30	462	26	392
Rectangular	15	213	11	167
	30	438	25	377
45° offset	15	221	13	194
	30	445	27	381
0° offset	15	220	11	156
	30	444	21	300
Flat Plate	15	214	13	162
	30	439	28	359

Table 4 contains the incident power on the apertures which corresponds to the specified flux
level. The values on the left correspond to the two flux levels on every part while air was flowing
at 50 SLPM. The values on the right correspond to the equivalent low and high flux levels which
yield similar outlet temperature at a 35 SLPM air flow rate.
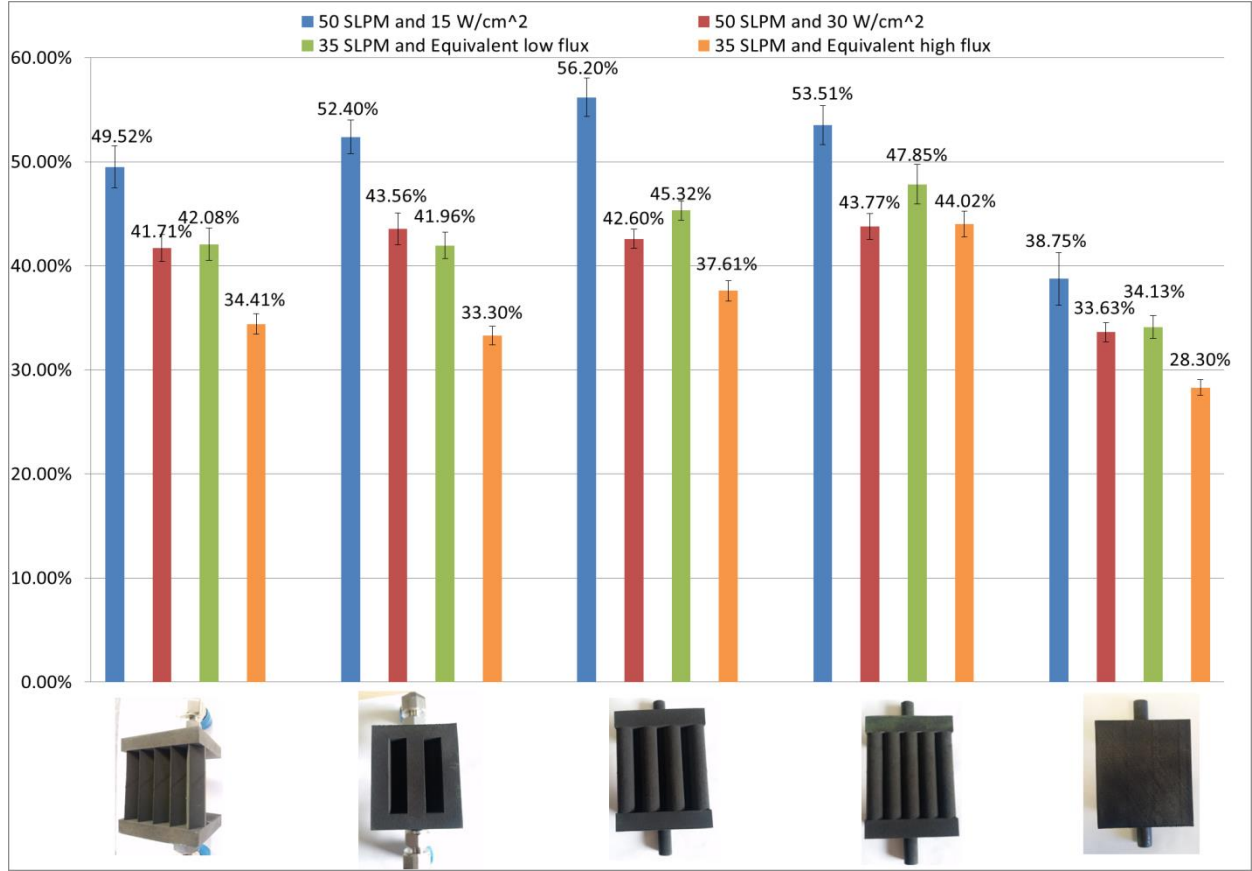
Figure 25. Thermal efficiency of FLGs. The equivalent high and low fluxes were estimated to match the outlet temperature of the 30 W/cm² and 15 W/cm² tests, respectively.

The absorbed heat was calculated as:

$$\dot{Q}_{abs} = \dot{m} \int_{T_{in}}^{T_{out}} C_p dT \tag{2}$$

Where $\dot{m}$ is the mass flow rate measured, Cp is the heat capacity of air as function of temperature and T_{in} and T_{out} are the measured inlet and outlet temperatures. Since there are small fluctuations in the measurements, the propagated error throughout our measurements was computed by means of the root sum squared (RSS) using Eq. (3).

$$\sigma_{sys} = \sqrt{\left(\sum_{i=1}^{n} \frac{\sigma_i}{\mu_i}\right)^2} \tag{3}$$

Where σ_{sys} is the equivalent standard deviation of the measurements, n is the number of variables, σ_i is the standard deviation of the individual variables and μ_i is the mean of the individual variable measurements. The RSS provides a general standard deviation for all the measurements combined.

Computational simulations using ANSYS Fluent were developed using the test results to tune the parameters specified. These models provide flexibility to analyze in detail the flow dynamics and the heat transfer across the FLGs. The goal of these models is to be able to predict the thermal efficiencies in the future by using the test results to fine-tune the models.

The k-ω Shear Stress Transport (SST) model was used to solve for the turbulent flow inside the FLGs. This model can accommodate a mesh with larger near-wall cells by handling Y+ values from 30 to 300. Initially the flow and turbulence equations were solved before the energy and radiation equations were enabled. Figure 26 shows the velocity contours of the air flow in different positions throughout the part.
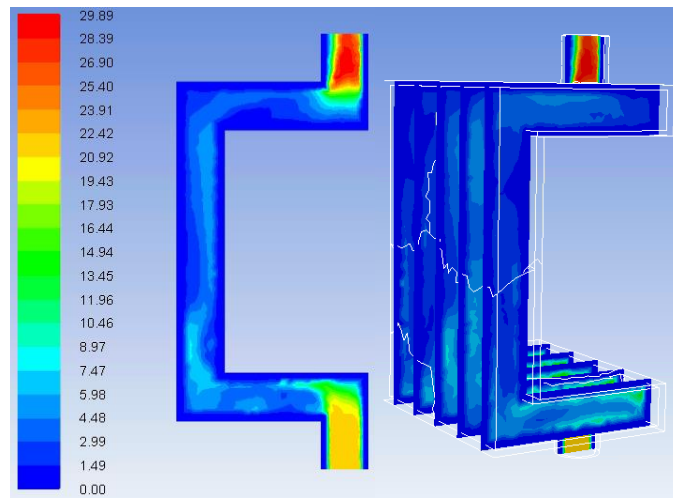
Figure 26. **Velocity contours of the air flow across the Flat Plate. Left: Central cross-sectional plane. Right: Five cross-sectional planes with one centimeter separation.**

The discrete ordinates radiation model was used to solve the conjugate heat transfer throughout the FLGs. Air is assumed to be a participating medium with an absorption coefficient of 0. Oxidized Inconel 718 has a measured emittance of 0.8 and a single band (i.e. infrared) is assumed.
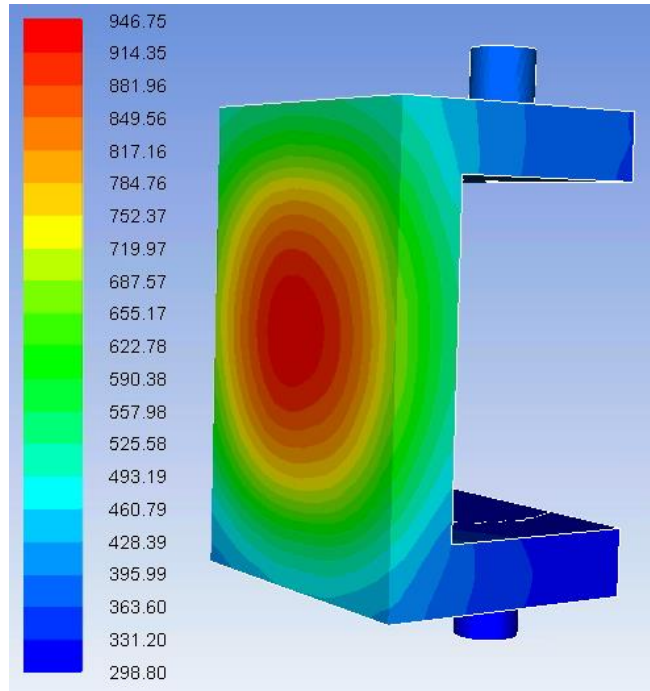
Figure 27. Temperature contour of the Flat Plate surface with an incident flux of 15 W/cm^2.
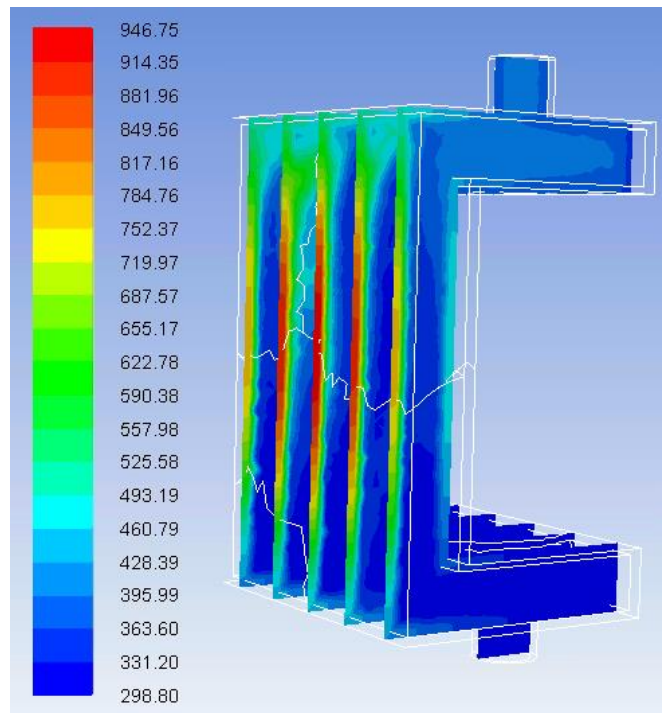
Figure 28. Temperature contours of the air flow across the Flat Plate with an incident flux of 15 W/cm^2. Five cross-sectional planes with one centimeter separation.
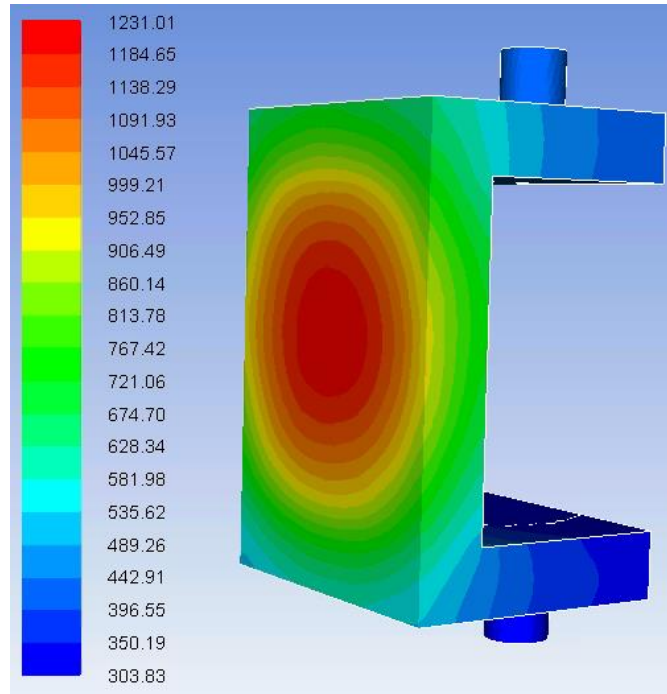
Figure 29. Temperature contour of the Flat Plate surface with an incident flux of 30 W/cm^2.
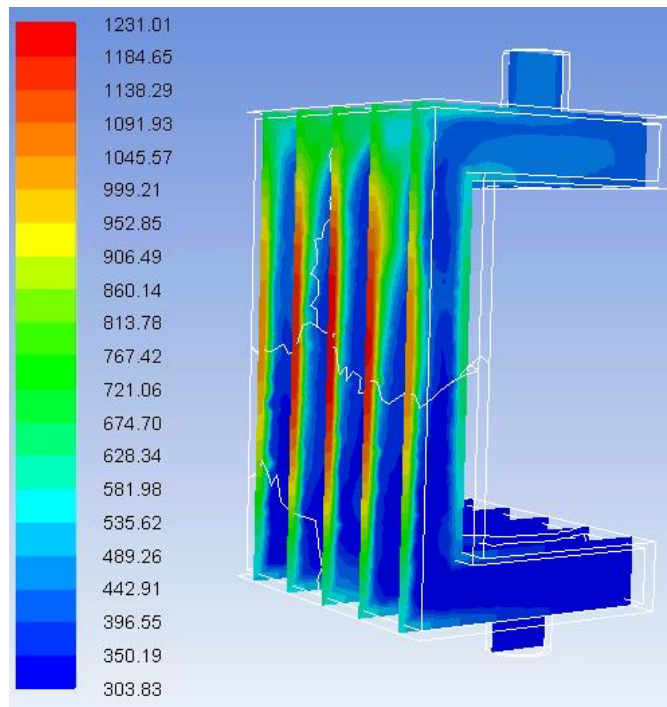
Figure 30. Temperature contours of the air flow across the Flat Plate with an incident flux of 30 W/cm^2. Five cross-sectional planes with one centimeter separation.

Figure 27 – Figure 30 show the temperature contours on the surface and in specific regions of the fluid zone inside the part. These temperatures are compared to the measured temperatures in the tests. Figure 31 and Figure 32 show the comparison between temperatures measured and temperatures modeled. In both figures, the temperatures correspond to the first 2 cases (i.e. 15 and 30 W/cm^2) and 50 SLPM air flow rate, respectively.
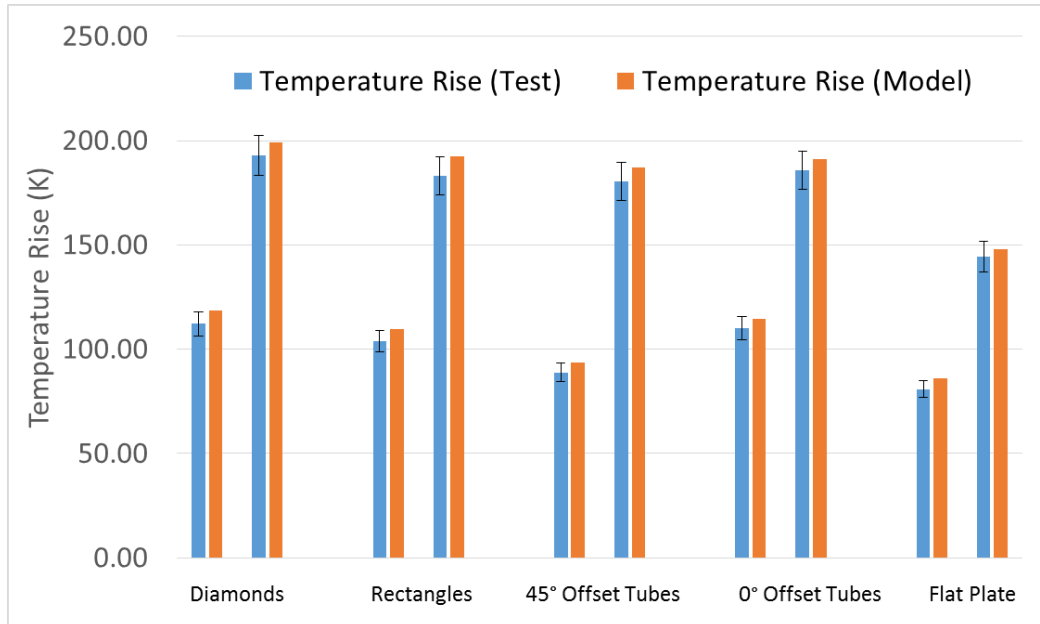
Figure 31. Measured and simulated air-temperature rise during tests of FLGs. Error bars represent the standard deviation on the measurements.
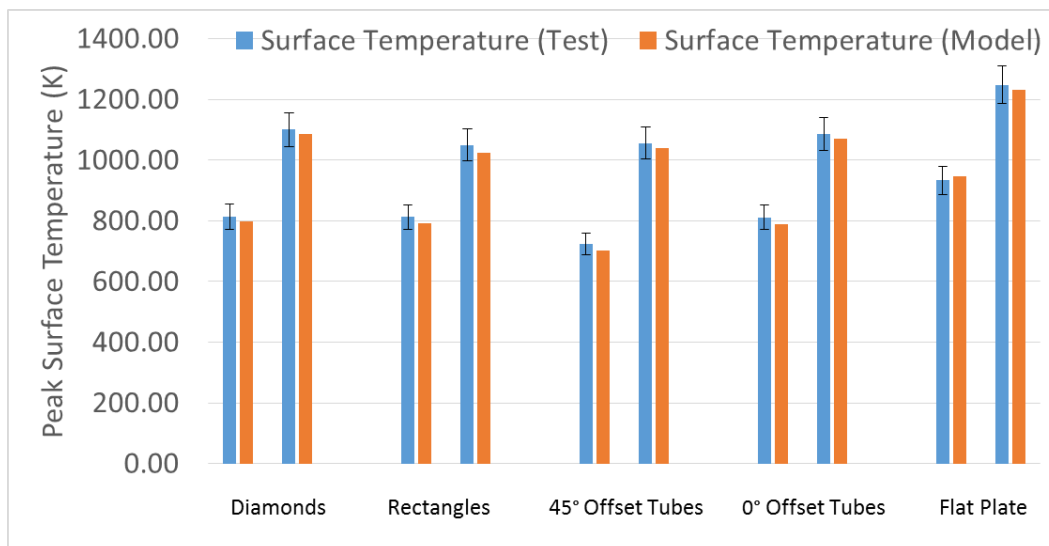
Figure 32. Measured and simulated peak surface temperatures during tests of FLGs. Error bars represent the standard deviation on the measurements.

The temperatures obtained from the models were found to be comparable to the ones measured in the tests. There are several reasons why the temperatures don't match exactly. First, there are some variations that occur from the wind in different days. This directly relates to the convective losses. Also, the heat transferred to the components in contact with the FLGs (i.e. connectors and mount), which was not accounted for in the models.

3.2 Macro-Scale Testing

Macro-scale testing was performed using the solar tower at the National Solar Thermal Test Facility (Figure 33). The tower is 61 m high with three test bays on the north-side of the tower (facing the heliostats) and a test structure on top of the tower. There are 218 heliostats (37 m^2) capable of producing 6 MW$_t$ power with associated flux levels up to 3000 suns. The lower test bay on the tower (220' level) was set up to accommodate small scale receiver testing. This test bay was utilized to test a flat panel (bill board) receiver design and the Bladed Receiver.

Figure 33. NSTTF solar tower and heliostats.

3.2.1 Design

The design of the thermal receiver followed the requirements specified for a pressure vessel in the *American Society of Mechanical Engineer Boiler and Pressure Vessel Code* (*ASME BPVC*). *Section VIII* (Pressure Vessel) was determined to be the most applicable since it considers higher operating temperatures and stress levels. Although it is known that the safety factors considered in the Section VIII might not be necessarily applicable to solar applications, it has lower safety factors than those in *Section I* (Boilers) and *Section III* (Nuclear Vessels).

The design pressure and temperatures were initially assumed to be close to the operating conditions that supercritical carbon dioxide (sCO$_2$) used by Ortega et al. [3]. The following design conditions were taken:

- Design Pressure: 20 MPa
- Design Temperature: 700°C
- Design Life: 100,000 hours of operation

3.2.1.1 Header Design Selection

As the number of tubes was determined from the optical modeling studies, the panels had a nominal size and configuration. The receiver configuration selected requires the back panels to have 13 tubes and the fins to have 18 tubes. In order to try and exploit the technical objective 2, the fins will be separated into two panels to explore the influence in localized "hot regions" throughout the receiver. Figure 34 shows the configurations of the two different panels were designed with the least differences. The spacing between the tubes was kept consistent to estimate the wall thickness of the headers. The headers were selected to be made out of 3" Inconel 625 pipe (3.5" or 88.9 mm O.D.) to have enough space for the tubes and be able to select the smallest thickness possible. Nonetheless, suppliers' stock is typically limited to schedule 40 and 80 in these alloys.

Back Panels (13 tubes)   Fin Panels (9 tubes)
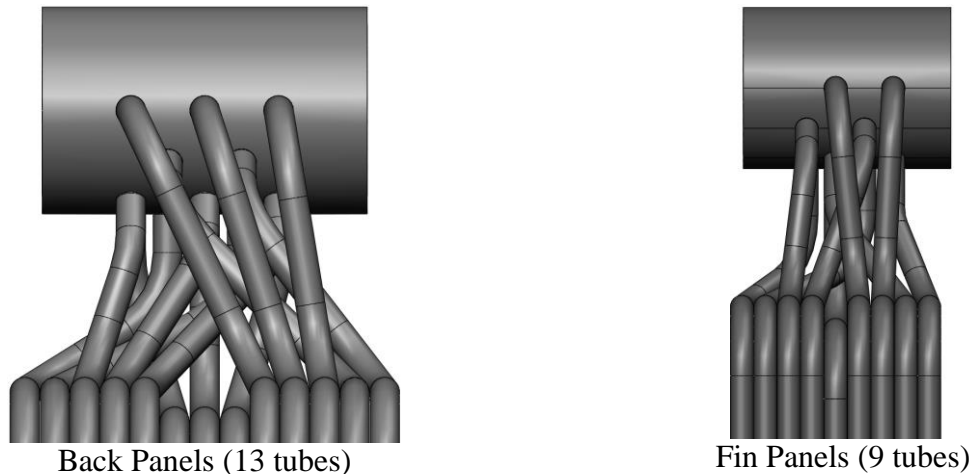
Figure 34.The manifolds were designed to accommodate the number of tubes for each panel.

As suggested by Ortega et al. [3] Inconel 625 was selected for this analysis, since the allowable stresses for the desired operating temperature are comparable to that of Haynes 230 or Inconel 617, but the availability of Inconel 625 makes it very suitable for solar applications. Figure 35 shows a comparison of Inconel 625 to other high-strength nickel alloys that could be used for high-temperature solar power applications.
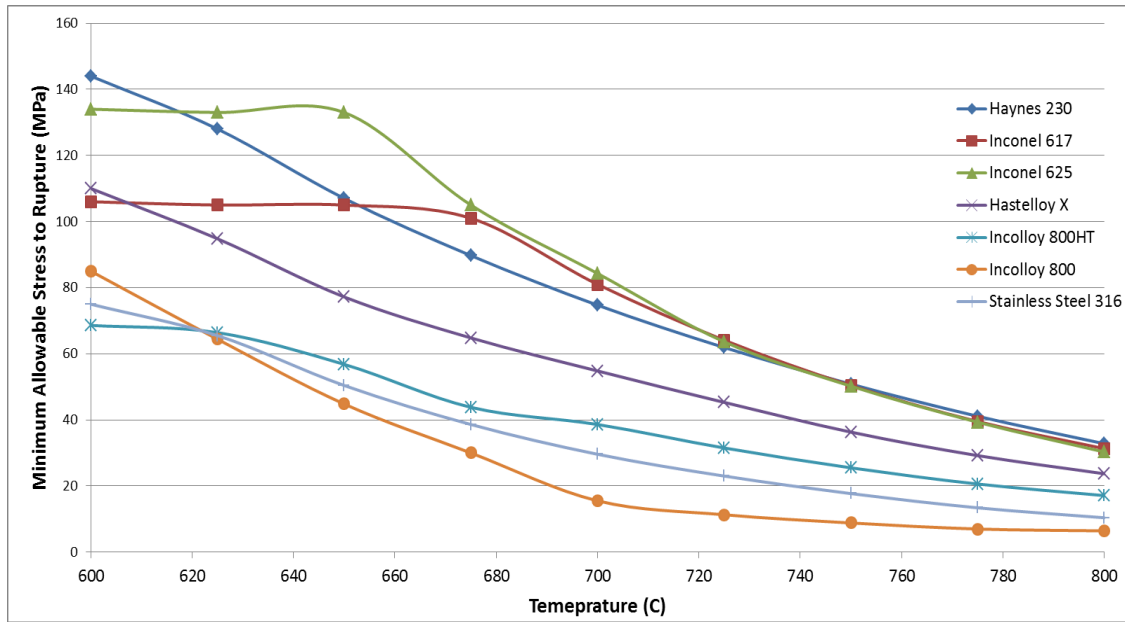
Figure 35. Maximum allowable stresses as a function of temperature. These values correspond to the 80% of the minimum creep rupture stress at 100,000 hours [4].

3.2.1.2 *ASME Section VIII* Design Methodology

The minimum thickness was estimated using the formulas in UG-27.

$$t = \frac{PR}{SE - 0.6P} \quad \text{or} \quad P = \frac{SEt}{R + 0.6t}$$

Where P is the design pressure, R is the internal radius of the vessel; S is the maximum allowable stress at operating temperature (Figure 35), and E is the ligament or joint efficiency. An extra corrosion allowance or manufacturing tolerance can be added, if necessary. This formula was used along with the design conditions for a 3" sch40 pipe and 3" sch80 pipe to calculate the minimum wall thicknesses required for a vessel shown in Table 6.

Similarly, the joint or ligament efficiency can be estimated from UG-53 by selecting the lowest of the efficiencies calculated based on the location of the holes (Figure 36.

43

Figure UG-53.4
Example of Tube Spacing With Tube Holes on
Diagonal Lines
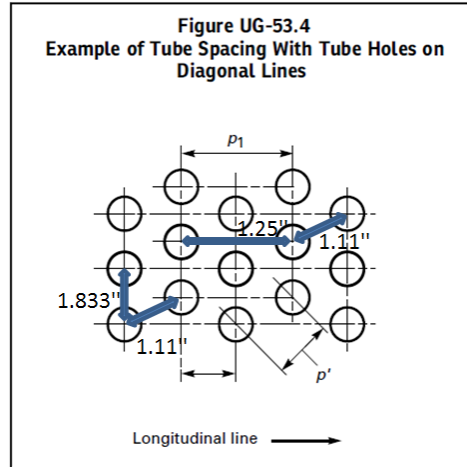
$$\text{Longitudinal efficiency, } \% = E_{\text{long.}} = [(p_1 - d)/p_1]\,100$$

$$\text{Diagonal efficiency, } \% = \frac{J + 0.25 - \left(1 - 0.01E_{\text{long.}}\right)\sqrt{0.75 + J}}{0.00375 + 0.005J}$$

$$J = (p'/p_1)^2$$

Figure 36. Longitudinal and diagonal efficiencies based on hole size and spacing.

Where d is the diameter of the tube holes, p_1 is the center to center distance of the longitudinal holes and p' is the center to center distance of the diagonal holes. Table 5 shows the ligament efficiencies calculated using the formulas above. Since the spacing of the holes was consistent in both headers, the calculation applied for both designs. The longitudinal efficiency was chosen as it is the lowest ligament efficiency.

Table 6 shows the calculated minimum wall thicknesses required by the initial design criteria.

Table 5. Ligament efficiencies calculated by UG-53

Ligament Efficiencies	
Tube Hole Diameter	12.7mm (1/2")
LONGITUDINAL PITCH (p)	31.75 mm (1.25")
LONGITUDINAL EFFICIENCY	60.00%
CIRCUMFERENTIAL PITCH	46.57 mm (1.833")
CIRCUMFERENTIAL EFFICIENCY	72.72%
DIAGONAL PITCH (p')	28.19 mm (1.11")
DIAGONAL EFFICIENCY	68.00%

Due to the limitation in pipe schedules, schedule 40 and 80 were analyzed. As observed in Table 6, the pipes are not sufficiently thick to operate at the initial design conditions. Even a 3" pipe schedule 160 would not be sufficient to meet the *Section VIII* requirements. It was determined that a 3" sch80 pipe would be used and the design temperatures and pressures would be adjusted

accordingly. Table 7 contains the values of the adjusted design conditions that the 3" pipe can sustain. These conditions are used to continue the rest of the design. The headers are considered our weakest component in the design.

Table 6. Minimum pipe thicknesses calculated by UG-27 at initial design conditions

3" sch40 pipe			3" sch80 pipe		
PIPE OD	88.9	mm	PIPE OD	88.9	mm
PIPE WALL	5.4864	mm	PIPE WALL	7.62	mm
INSIDE RADIUS	38.9636	mm	INSIDE RADIUS	36.83	mm
DESIGN PRESSURE	20	MPa	DESIGN PRESSURE	20	MPa
DICTICATING EFFICIENCY	0.6		DICTICATING EFFICIENCY	0.6	
CORROSION ALLOWANCE	-	mm	CORROSION ALLOWANCE	-	mm
MANUFACTURING TOLERANCE	0.127	mm	MANUFACTURING TOLERANCE	0.127	mm
DESIGN TEMPERATURE	700	°C	DESIGN TEMPERATURE	700	°C
ALLOWABLE STRESS	84.3	MPa	ALLOWABLE STRESS	84.3	MPa
MINIMUM THICKNESS	20.3	mm	MINIMUM THICKNESS	19.2	mm

Table 7. Minimum pipe thicknesses calculated by UG-27 at adjusted design conditions.

3" sch80 pipe		
PIPE OD	88.9	mm
PIPE WALL	7.62	mm
INSIDE RADIUS	36.83	mm
DESIGN PRESSURE	15	MPa
DICTICATING EFFICIENCY	0.6	
CORROSION ALLOWANCE	-	mm
MANUFACTURING TOLERANCE	0.127	mm
DESIGN TEMPERATURE	650	°C
ALLOWABLE STRESS	137.9	MPa
YIELD STRESS	275	MPa
MINIMUM THICKNESS	7.62	mm
MAXIMUM ALLOWABLE WORKING PRESSURE	15.2	MPa
MEMBRANE STRESS	135.8	MPa
TEST PRESSURE	26.1	MPa
MEMBRANE STRESS AT TEST PRESSURE	236.6	MPa

The maximum allowable working pressure (MAWP), the membrane stress and the test pressures can be estimated by:

$$MAWPpipe = \frac{SEt}{R + (.6t)}$$

$$MEM.STRESS = \frac{P(R+.6t)}{Et}$$

$$Ptest = 1.3rP$$

Where P is the design pressure, R is the internal radius of the vessel; S is the maximum allowable stress (MAS) at operating temperature, t is the pipe wall thickness and r is the ratio of the MAS at test temperature and MAS at design temperature. The calculation results can be found in Table 7. Since the MAWP is higher than the design pressure, the design pressure can be the operating pressure. The membrane stress is the maximum stress that the pipe will experience at the design conditions specified in Table 7. Lastly, the test pressure is performed to assure that the component can safely operate at the operating conditions. It is important to check that the membrane stress at test pressure is below the 90% of the Yield Strength.

3.2.1.3 Tube Design Selection

Knowing the design constraints, the tube design process is similar to that of the header pipe. Figure 37 shows the tubes connecting to the manifold of every panel. The same design conditions are used in the tubes. Table 8 contains the results of the calculations based on the UG-27 and UG-53 equations for the tubes and pipe connecting to the header.

Back Panels (13 tubes)   Fin Panels (9 tubes)
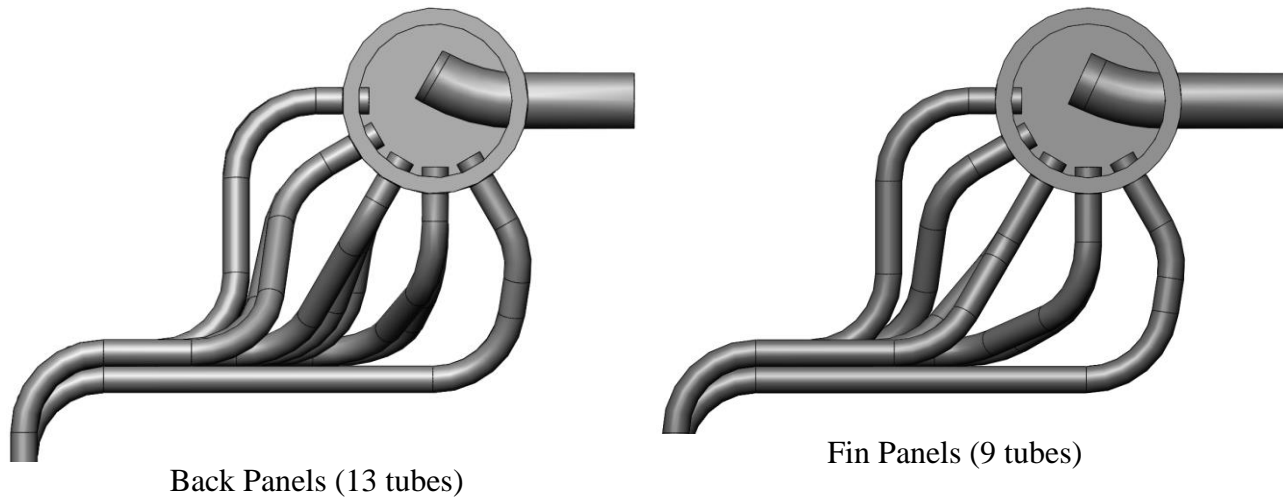
Figure 37. The tubes were designed to accommodate the number on every manifold.

Based on the new design criteria chosen, all the components meet the minimal requirements specified in *Section VIII*.

Table 8. Minimum thicknesses calculated by UG-27 at the same design conditions as the header pipe.

1/2" Tube			3/4" sch40 pipe		
PIPE OD	12.7	mm	**PIPE OD**	26.67	mm
PIPE WALL	1.651	mm	**PIPE WALL**	2.8702	mm
INSIDE RADIUS	4.699	mm	**INSIDE RADIUS**	10.4648	mm

1/2" Tube			3/4" sch40 pipe		
DESIGN PRESSURE	15	MPa	DESIGN PRESSURE	15	MPa
DICTICATING EFFICIENCY UG-53	1		DICTICATING EFFICIENCY UG-53	1	
CORROSION ALLOWANCE	-	mm	CORROSION ALLOWANCE	-	mm
MANUFACTURING TOLERANCE	0.127	mm	MANUFACTURING TOLERANCE	0.127	mm
DESIGN TEMPERATURE	650	°C	DESIGN TEMPERATURE	650	°C
ALLOWABLE STRESS	137.9	MPa	ALLOWABLE STRESS	137.9	MPa
YIELD STRESS	275	MPa	YIELD STRESS	275	MPa
MINIMUM THICKNESS	0.67	mm	MINIMUM THICKNESS	1.34	mm
MAXIMUM ALLOWABLE WORKING PRESSURE	40.02	MPa	MAXIMUM ALLOWABLE WORKING PRESSURE	32.48	MPa
MEMBRANE STRESS	51.69	MPa	MEMBRANE STRESS	63.69	MPa
TEST PRESSURE	26.13	MPa	TEST PRESSURE	26.13	MPa
MEMBRANE STRESS AT TEST PRESSURE	90.05	MPa	MEMBRANE STRESS AT TEST PRESSURE	110.95	MPa

3.2.1.4 End Cap Design

A similar design procedure using the same design conditions is required for the end caps of the headers. These caps are chosen to be flat, instead of ellipsoidal, to reduce the costs and lead time of manufacturing. UG-34 shows the procedure to estimate the required thickness of a flat head cover.

$$t = d \sqrt{CP \;/\; SE}$$

Where d is the internal diameter, C is the attachment coefficient, P is the design pressure, S is the maximum allowable stress at operating temperature (Figure 35), and E is the ligament or joint efficiency. Table 9 contains the results of the design calculations. A 19.05 mm (3/4") thick plate had to be chosen since the suppliers did not carry 15.875 mm (5/8") which could have been closer to the minimum thickness required.

Table 9.Minimum thicknesses calculated by UG-27 and UG-34 at the same design conditions as the header pipe.

¾" Plate		
PIPE OD	88.9	mm
PIPE WALL	7.62	mm
INSIDE RADIUS	36.83	mm
DESIGN PRESSURE	15	MPa
DICTICATING EFFICIENCY UG-53	0.85	
CORROSION ALLOWANCE	-	mm
MANUFACTURING TOLERANCE	0.127	mm
ATTACHEMENT COEFFICIENT	0.3	

¾" Plate		
DESIGN TEMPERATURE	650	°C
ALLOWABLE STRESS	137.9	MPa
MINIMUM THICKNESS	14.56	mm
PLATE THICKNESS	19.05	mm
MAXIMUM ALLOWABLE WORKING PRESSURE	104.53	MPa
MEMBRANE STRESS	44.71	MPa
TEST PRESSURE	26.13	MPa
MEMBRANE STRESS	77.88	MPa

Header with tubes inserted before welding

Caps in place before welding
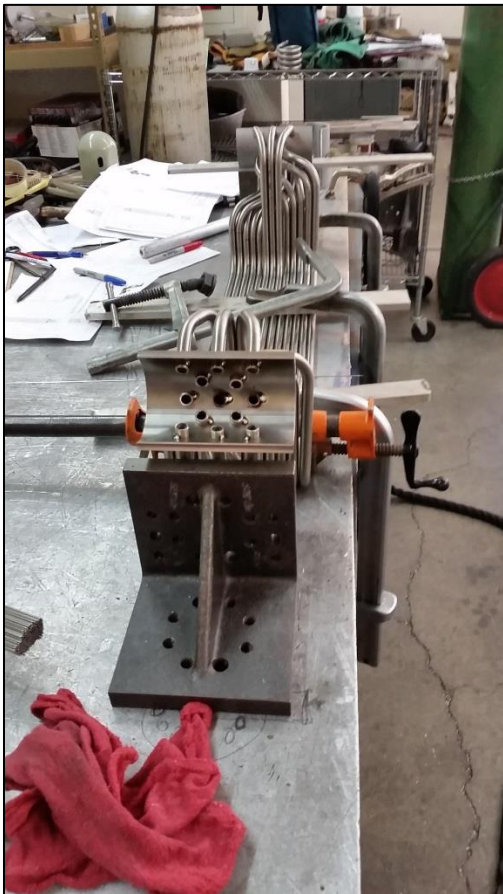
Back Panel (13 tubes) assembled and tacked in place

Fin Panels (9 tubes each) assembled and tacked in place

Figure 38. Assembly and weld preparation of panels.

3.2.1.5 Weld Design and Reinforcement

The weld design requirements for the area of reinforcement can be found in UG-37 while the weld strength analysis is located in UG-41 of *Section VIII*. Figure 39 contains the information required to estimate the amount of area required for the welds of the tubes.

Figure UG-37.1
Nomenclature and Formulas for Reinforced Openings

GENERAL NOTE:
Includes consideration of these areas if
$S_n/S_v < 1.0$ (both sides of ₵)

2.5t or 2.5t_n + t_e
Use smaller value

h, 2.5t, 2.5t_i
Use smallest value

See UG-40
for limits of
reinforcement

d or $R_n + t_n + t$
Use larger value

d or $R_n + t_n + t$
Use larger value

For nozzle wall inserted through the vessel wall ⟶ ⟵ For nozzle wall abutting the vessel wall

Without Reinforcing Element

$A = d\,t_r\,F + 2t_n\,t_r\,F(1 - f_{r1})$ — Area required

$A_1 \begin{cases} = d(E_1 t - F t_r) - 2t_n (E_1 t - F t_r)(1 - f_{r1}) \\ = 2(t + t_n)(E_1 t - F t_r) - 2t_n (E_1 t - F t_r)(1 - f_{r1}) \end{cases}$ — Area available in shell; use larger value

$A_2 \begin{cases} = 5(t_n - t_{rn})\,f_{r2}\,t \\ = 5(t_n - t_{rn})\,f_{r2}\,t_n \end{cases}$ — Area available in nozzle projecting outward; use smaller value

$A_3 \begin{cases} = 5t\,t_i\,f_{r2} \\ = 5t_i\,t_i\,f_{r2} \\ = 2h\,t_i\,f_{r2} \end{cases}$ — Area available in inward nozzle; use smallest value

$A_{41} = \text{outward nozzle weld} = (\text{leg})^2 f_{r2}$ — Area available in outward weld

$A_{43} = \text{inward nozzle weld} = (\text{leg})^2 f_{r2}$ — Area available in inward weld

If $A_1 + A_2 + A_3 + A_{41} + A_{43} \geq A$ — Opening is adequately reinforced

If $A_1 + A_2 + A_3 + A_{41} + A_{43} < A$ — Opening is not adequately reinforced so reinforcing elements must be added and/or thicknesses must be increased

With Reinforcing Element Added

A = same as A, above — Area required

A_1 = same as A_1, above — Area available

$A_2 \begin{cases} = 5(t_n - t_{rn})f_{r2}t \\ = 2(t_n - t_{rn})(2.5t_n + t_e)f_{r2} \end{cases}$ — Area available in nozzle projecting outward; use smaller area

A_3 = same as A_3, above — Area available in inward nozzle

$A_{41} = \text{outward nozzle weld} = (\text{leg})^2 f_{r3}$ — Area available in outward weld

$A_{42} = \text{outer element weld} = (\text{leg})^2 f_{r4}$ — Area available in outer weld

$A_{43} = \text{inward nozzle weld} = (\text{leg})^2 f_{r2}$ — Area available in inward weld

$A_5 = (D_p - d - 2t_n)\,t_e\,f_{r4}$ [Note (1)] — Area available in element

If $A_1 + A_2 + A_3 + A_{41} + A_{42} + A_{43} + A_5 \geq A$ — Opening is adequately reinforced

GENERAL NOTE: This figure illustrates a common nozzle configuration and is not intended to prohibit other configurations permitted by the Code.

NOTE:
(1) This formula is applicable for a rectangular cross-sectional element that falls within the limits of reinforcement.

Figure 39. Figure of UG-37.1 used to estimate the area available of the weld.

3.2.1.6 Tube Welds

The area of reinforcement of the tubes penetrating the header pipe, shown in Figure 40, is calculated using the methodology shown in Figure 39. The results of the calculations using the values in Table 7 and Table 8 are shown in Cap Welds

50

Referencing the values from Table 9, the minimum weld size required is the at least the size of the header wall. The weld chosen was a single-butt partial-penetration weld as shown in Figure 42.

Simplified diagram of the partial-penetration weld of the Caps and Header pipe

The Caps on the Header
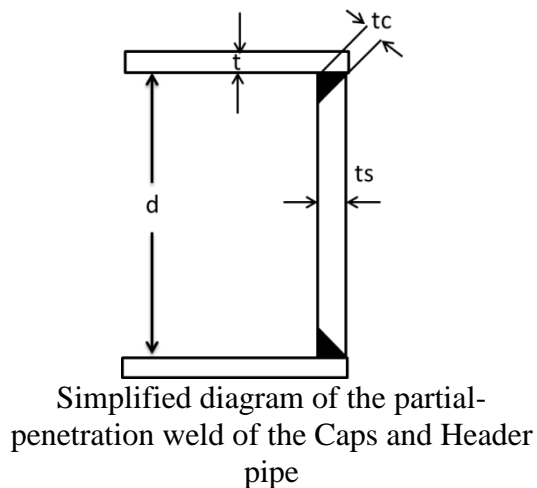
Figure 42. Single-butt partial-penetration welds in for the caps and headers.

Table 11. Weld size selection values for a full penetration weld.

Single-butt partial-penetration welds		
t (header wall thickness -manufacturing tolerance)	7.49	mm
Weld size required	7.49	mm
Weld size selected (full penetration weld)	9.525	mm

In both instances, the area available is larger than the area required which means no further reinforcement is required.

Simplified diagram of the internal weld of the tubes penetrating the header pipe.

Tubes penetrating the header pipe.

Figure 40. Tube projection inside header pipe.

| Internal Weld on the Tubes | External Weld on Pipes |

Figure 41. Welds required to join the tubes and pipes to the header pipe.

Table 10. Area of Reinforcement Calculations for ½" tubes and ¾" pipe penetrating the header pipe.

	1/2" Tube	3/4" Pipe	
Area Available Required			
Sv (allowable stress of header)	137.90	137.90	MPa
Sn (allowable stress of tube)	137.90	137.90	MPa
Sp (allowable stress of reinforcing element)	137.90	137.90	MPa
t (header wall thickness - manufacturing tolerance)	7.49	7.49	mm
tr (required thickness of seamless header)	4.29	4.29	mm
d (inside tube diameter)	9.40	20.93	mm
tn (tube wall thickness)	1.65	2.87	mm
trn (tube thickness of seamless header)	0.67	1.34	mm
ti (tube thickness projecting inside header)	1.65	1.65	mm
h (projection inside header)	3.18	3.18	mm
fr1=Sn/Sv	1.00	1.00	
E1 (opening factor)	1.00	1.00	
F (correction factor for internal pressure variation)	1.00	1.00	
fr2= Sn/Sv	1.00	1.00	
fr3 (lesser of Sn or Sp)/Sv	1.00	1.00	
fr4= Sp/Sv	N/A	N/A	
A=dtrF+2tntrF(1-fr1) (minimum area required)	40.35	89.85	mm^2
Area Available Without Reinforcing Element			
A1=d(E1t-Ftr)-2tn(E1t-Ftr)(1-fr1)	30.07	66.98	mm^2
A1=2(t+tn)(E1t-Ftr)-2tn(E1t-Ftr)(1-fr1)	58.52	66.32	mm^2
A1 (area available in header; largest value of A1)	58.52	66.98	mm^2

	1/2" Tube	3/4" Pipe	
A2=5(tn-trn)fr2t	36.75	57.32	mm^2
A2=5(tn-trn)fr2tn	8.10	21.96	mm^2
A2 (area available in tube; smallest value A2)	8.10	21.96	mm^2
A3=5ttifr2	61.85	61.82	mm^2
A3=5titifr2	13.63	13.61	mm^2
A3=2htifr2	10.48	10.48	mm^2
A3 (area available in tube extension; smallest value A2)	10.48	10.48	mm^2
l (minimum weld size)	3.18	3.18	mm
A41=l^2*fr3 (outward nozzle weld)	10.08	10.08	mm^2
A43=l^2*fr2 (inward nozzle weld)	10.08	10.08	mm^2
A1+A2+A3+A41+A43 > A	97.26	119.57	mm^2

3.2.1.7 Cap Welds

Referencing the values from Table 9, the minimum weld size required is the at least the size of the header wall. The weld chosen was a single-butt partial-penetration weld as shown in Figure 42.

Simplified diagram of the partial-penetration weld of the Caps and Header pipe
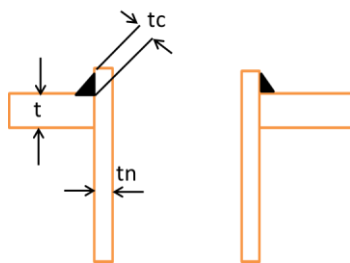

The Caps on the Header

Figure 42. Single-butt partial-penetration welds in for the caps and headers.

Table 11. Weld size selection values for a full penetration weld.
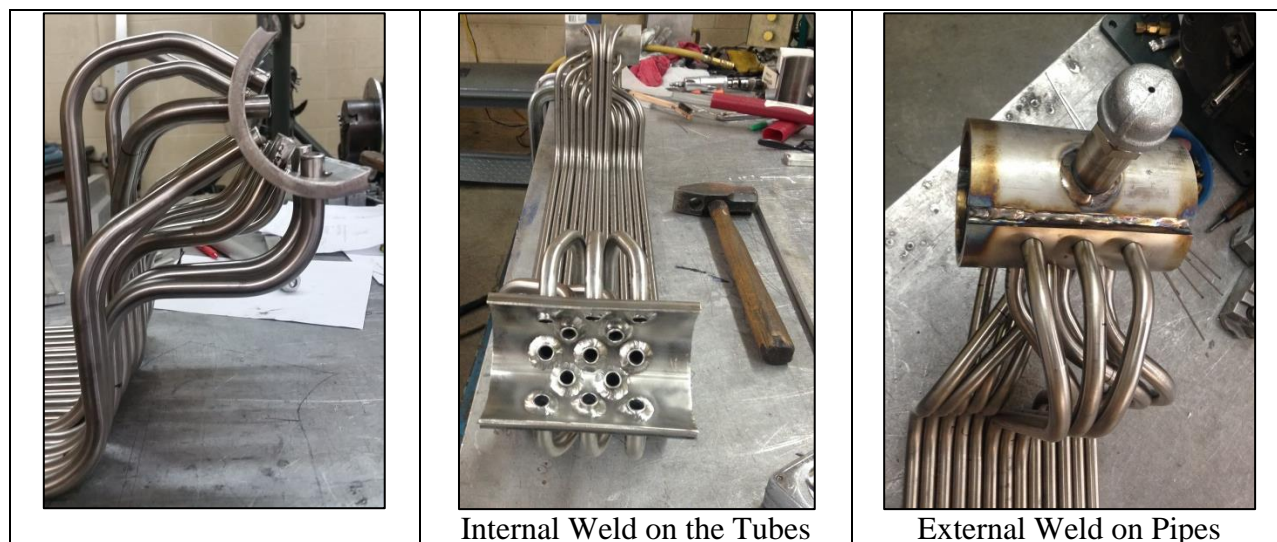
Single-butt partial-penetration welds		
t (header wall thickness -manufacturing tolerance)	7.49	mm
Weld size required	7.49	mm
Weld size selected (full penetration weld)	9.525	mm

3.2.1.8 Header Welds

The header pipes were cut into two longitudinal halves to perform the tube welds internally. This procedure does not affect the performance of the headers since the ligament efficiency is already 60%. The efficiency will remain the same as long as the seam weld, to join the halves, is fully penetrating as per UW-12 requirements. The joint efficiency of a full-penetration weld is 90% and 100% (by UW-12) if it is analyzed using a full-radiography method. J-grooves allow for a best full-penetration as shown in Figure 43.

Simplified diagram of the full-penetration weld along the seam of the header pipe

The full-penetration weld was performed under a Helium atmosphere.

The full penetration can be observed in the circled areas on the header
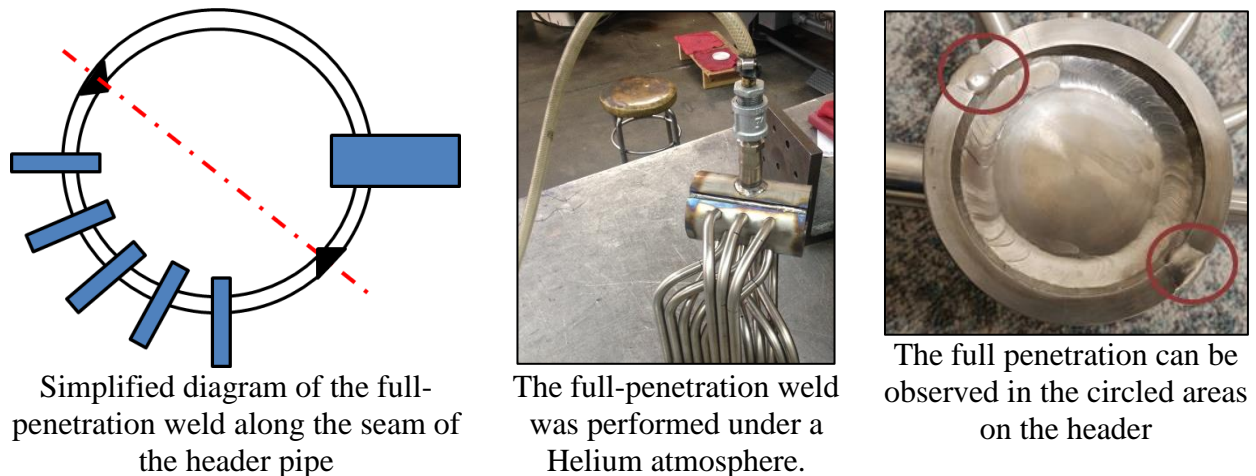
Figure 43. J-groove full-penetration welds in for the caps and headers.

The bending and cutting of the Inconel 625 tubes and pipes was performed by Springs Fabrication and Albina Inc. (Figure 44). The manufacturing of the Inconel 625 panels had to be done by a certified machine shop since it is considered a pressure vessel (Figure 45). The certification was completed by *ASME BPVC Section VIII* Standards.

Headers cut by Springs Fabrication
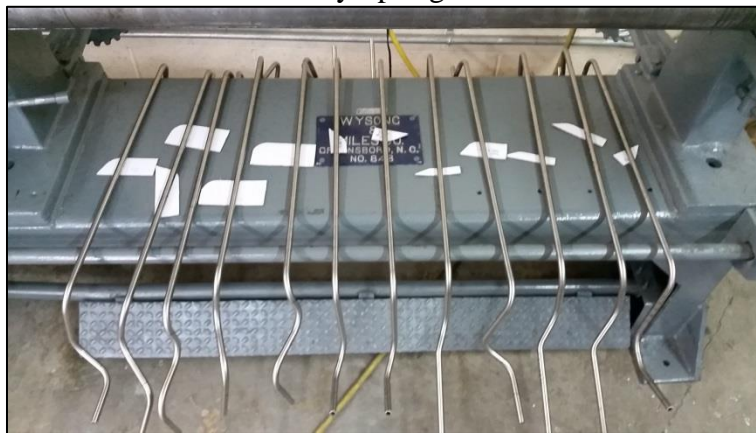
First set of 13 tubes needed for the back panels, bent by Albina, Inc

Figure 44. Tubes and pipes cut and bent for all the panels.

Dave Saavedra from Saavedra Precision Welding
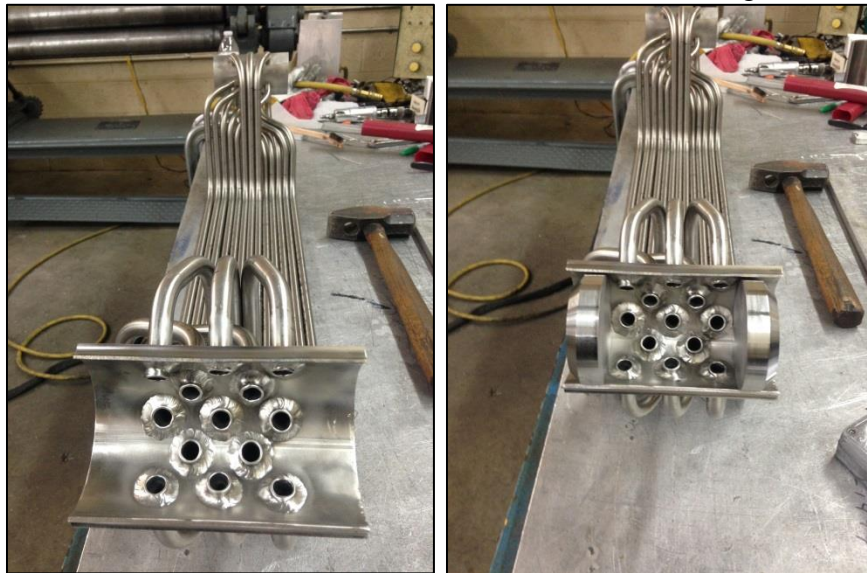
Internal Welds of all components
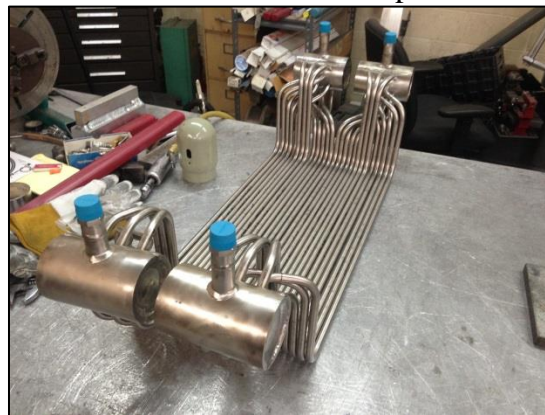
Completed panels
Figure 45. Building and welding of the tubular panels.

3.2.2 Solar Flux Distribution

The flux distribution was based on the heliostats chosen for providing power to the receiver. The NSTTF heliostat field is shown in Figure 46. Various combinations of heliostats that were evaluated by ray tracing are shown in the blue and red boxes.
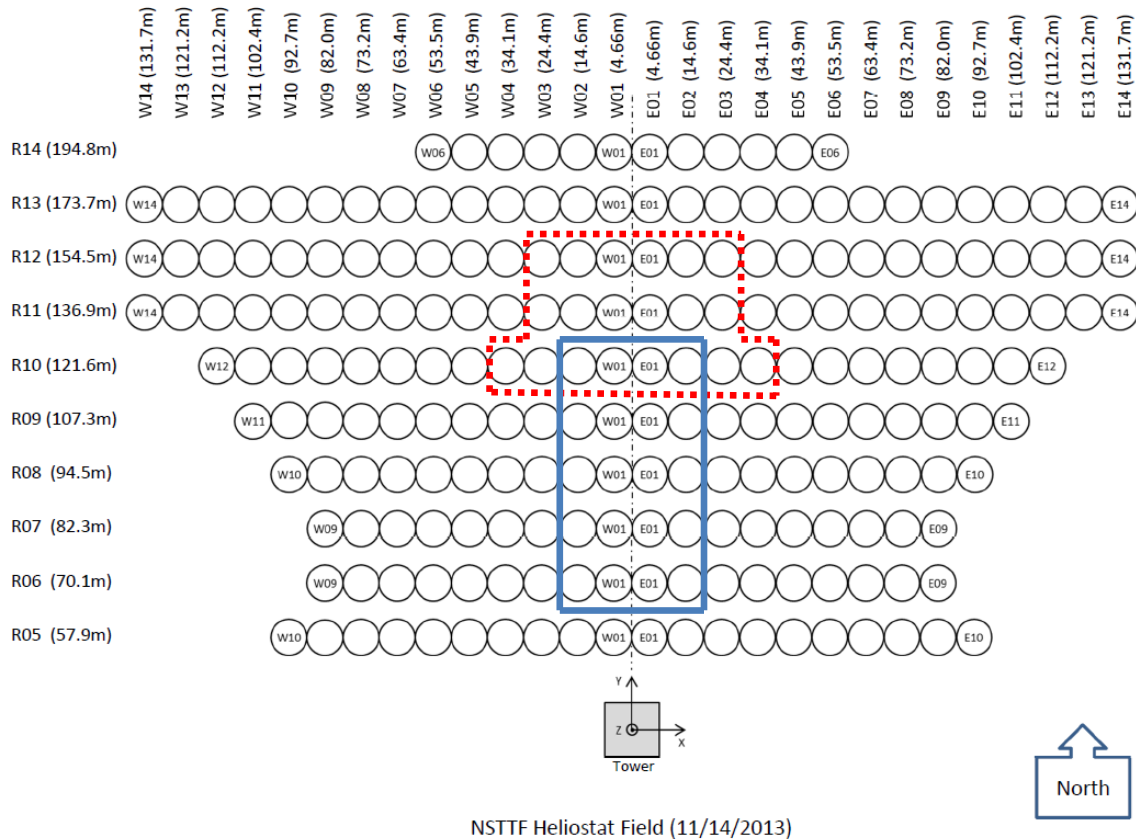
Figure 46. NSTTF heliostat field map with ray-trace and other possible heliostat configurations for prototype testing; red box (dashed lines) indicates ray trace heliostats; blue box (solid lines) indicates possible alternative heliostat configuration.

This prototype testing used air as the heat transfer fluid (HTF) in the receiver. Air is advantageous as it can be expelled to ambient, even when heated to extreme temperatures if needed. A continuous duty, high pressure air compressor is expected to be used with the system. The receiver is being designed to accommodate possible air or super-critical carbon dioxide cycles which require the HTF to operate at 10 MPa or above. Initially, the system is planned to be tested at ambient pressures which still allows the wall temperatures of the tubes to achieve temperatures of ~700°C or higher which is important when considering thermal re-radiation to the fin surfaces of the receiver. The thermal analysis is being performed for air as the HTF in the receiver tubes as well as using super-critical CO_2 which would be utilized in a commercial receiver.

There are three critical criteria that need to be met during on-sun testing of receivers:

1. The incident flux on the receiver needs to be measured and characterized.

2. The non-heated regions of the test apparatus and surrounding test bay need to be protected from high flux conditions.

3. The apparatus needs to be accessible for repairs and measurement devices.

The incident flux on the receiver will be measured through the use of a "flux panel". The flux panel is a water/glycol cooled target composed of aluminum rectangular tubing. The tubing is stacked and joined with 180° tube elbows to form a serpentine pattern. The cooling fluid flows into the target at the lowest tube and serpentines to the outlet at the top of the panel. At the center of the panel design is a Kendall radiometer capable of accurate heat flux measurements. This flux gage is used to calibrate images taken of the flux panel when a heliostat beam is applied. A picture is taken of the flux and then each pixel is scaled according to the measurement of the sensor. The picture can then be used to determine the incident power on the target. The receiver is then directly to the right of this flux panel. It is assumed that the measured incident power on the flux panel is nearly identical to the incident power on the receiver directly after the beam moves. A power measurement is taken before and after exposure to the receiver.
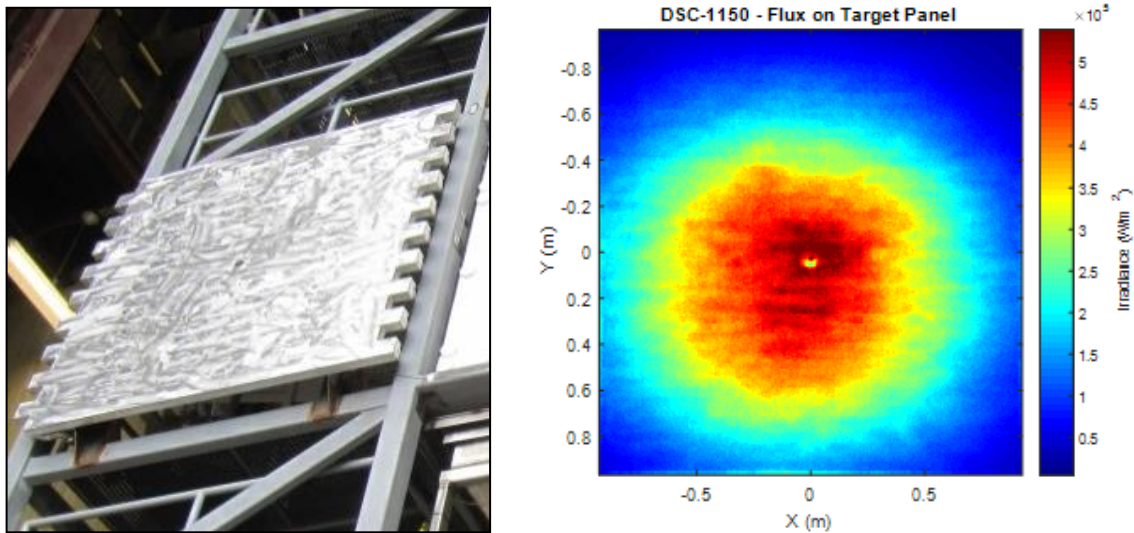
Figure 47. (left) Flux panel fabricated at the NSTTF; (right) flux image taken on the flux panel seen to the left.

3.2.3 On-Sun Testing
Two receivers were tested at the 220 ft. level (120 feet above ground level) of the solar tower at the National Solar Thermal Test Facility (NSTTF) (Figure 48). The system used air as a heat transfer medium that was provided by an oil-free compressor at the ground level of the Solar Tower. A flat panel receiver acted as the baseline receiver case as it is typical of receiver panel arrangements in existing CSP plants. The bladed panel receiver consisted of the flat panel receiver, but also included "blades" arranged at a 50° angle from vertical to trap the incoming irradiation from the heliostat field. The ray tracing and CFD simulations predict that light

trapping is increased with the bladed designs causing an increase in thermal efficiency of the receiver. The flat panel receiver was tested on-sun on 09/09/2016. After this test, the rig was modified to hold the bladed panels in place and was tested on 09/19/2016.
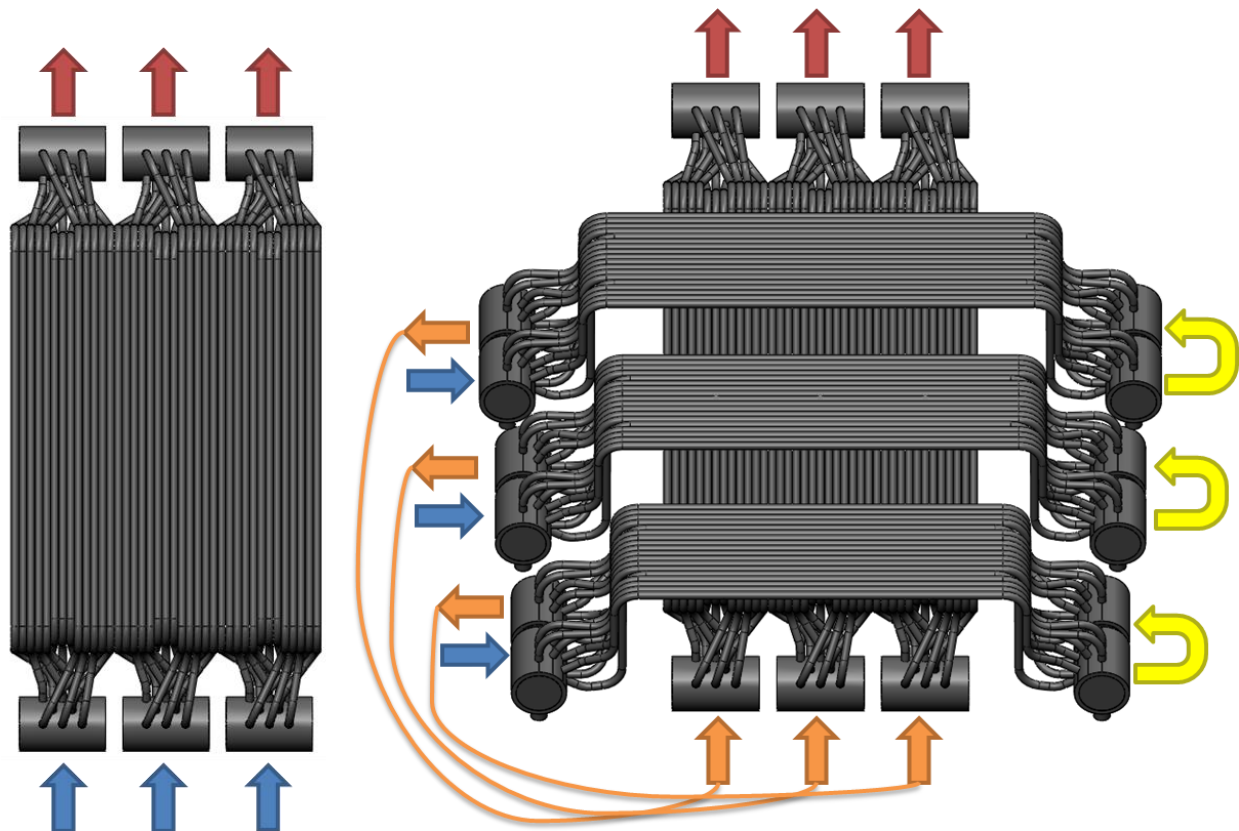
Figure 48. Flat (left) and bladed (right) receiver configurations tested on-sun.

3.2.3.1 Test procedure
The following test procedure was followed for each test:

1. Initiate heliostat field start-up
2. Inspect test rig and ensure all connections are secure and apparatus is secured in rig
    a) Connect/Power UPS to power DAQ
    b) Plug Ethernet cable
    c) Power mass flow meters
    d) Ensure all connections are proper
3. Start-up cooling pumps and water cooling for flux gauge and flux target and start tower NIP
4. Ensure camera monitor in test bay is working properly
5. Turn on compressor (will take about 20 seconds to start loading)
    a) Close valve to fill tank (120-125 psi)
    b) Open the tank's valve to pressurize the system (115-120 psi)
    c) Check the mass flow rate/pressure readings

d) Valves will require little/no adjustment
6. Secure test bay and turn test in progress lights on
7. Make site announcement
8. Start collecting data and ensure values appear correct
9. Start recording data
10. Bring heliostats to calibration panel to record pre-test irradiance and DNI
11. Move heliostat beams to receiver
12. Monitor thermocouples and sensors and wait to achieve steady-state
13. Take PHLUX image
14. Once steady-state has been achieved for at least several minutes, move beams back to calibration panel to get post-test irradiance
15. Repeat steps 11 - 14 multiple times to get repeatability data
    a) Note: DNI may be changing during this time
16. We can adjust the mass flow rate using valves and repeat the test procedure at a different mass flow rate (Optional)
17. Shut down heliostat field
18. Shut down compressor and vent out the air in the tank
    a) Open vent and drain valves on air tank
19. Power down DAQ and mass flow meters
    a) Do not close flow meter valves
    b) Do not disconnect anything from the DAQ
20. Make site announcement and turn test in progress lights off

The heliostat beams were added to the receiver one at a time to avoid thermal shock in the receiver panels. This was done until the final irradiance was on the receiver and then the system was allowed to achieve thermal equilibrium. The thermal equilibrium was determined when the temperatures in the system were all "flat-lined" achieving a steady state temperature. The mass flow rates and pressures in the outlet and inlet were monitored during testing to ensure that the system was operating as expected.

The incident flux on the receiver was measured through the use of a water cooled "flux panel". The flux panel is a water/glycol cooled target composed of aluminum rectangular tubing. The tubing is stacked and joined with 180° tube elbows to form a serpentine pattern. The cooling fluid flows into the target at the lowest tube and serpentines to the outlet at the top of the panel. At the center of the panel design is a flux gauge capable of accurate heat flux measurements up to 800 kW/m2. The back of the structure is seen in Figure 54. This flux gauge is used to calibrate images taken of the flux panel when a heliostat beam is applied. The heliostat beams are centered on the flux gauge on the flux panel. A picture is taken of the flux and then each pixel is scaled according to the measurement of the sensor. The picture can then be used to determine the incident power on the target. The receiver is then directly to the right of this flux panel. It is assumed that the measured incident power on the flux panel is nearly identical to the incident power on the receiver directly after the beam moves. A power measurement is taken before and after exposure to the receiver.

A Failure Modes Effects Analysis (FMEA) was performed as part of the safety engineering process used at SNL. Two major items were identified in the FMEA that were addressed. The

first item was that the test bay should be monitored at all times during testing. This was accomplished by using a Logitech Webcam plugged into a site stand-alone lab computer. During testing, off-gasing from the spillage boards were observed with this camera. The camera also ensured that no one was in the test bay during on-sun conditions. The second item was the need for a detailed Pressure Safety Data Package (PSDP). The PSDP was created and approved by a pressure safety advisor, ES&H specialist, and the Solar Tower manager.

3.2.3.2 Panel pre-oxidation

Inconel 625 sample coupons were oxidized and their reflectivity was measured. The oxidation was done at 800°C for different times as shown in Table 12. The goal was to oxidize the panels to achieve an intrinsic solar absorptance of ~0.9 (solar reflectivity ~0.1). The oxidation of the panels was performed in a high volume furnace shown in Figure 49.

Table 12. Reflectivity measurements of Inconel 625 oxidized samples. The last measurement was done on the flat caps of the panels oxidized.

Sample Oxidation			
Sample	Temperature (°C)	Time (hrs.)	Reflectivity
1	25	As received	0.519 ± 0.007
2	800	1	0.208 ± 0.006
3	800	5	0.18 ± 0.001
4	800	24	0.151 ± 0.001
Panel	800	30	0.124 ± 0.004

Figure 49. Furnace used to oxidize the panels for 30 hours at 800°C

Figure 50. Sample 1 and Sample 4 from Table 12.

3.2.3.3 Leading tube failure prevention

The leading edge/tube of the bladed receiver panels is subject to very high solar fluxes relative to the rest of the tubes due to higher view factors. Modeling was performed to evaluate the potential temperature rise of the front tube to determine of overheating might occur. The simulated average temperature rise of the tube surface with air flowing at a mass flow rate of ~3 g/s, outlet pressure of 455 kPa, and irradiance of 300 kW/m^2 was ~100 °C with a peak temperature rise of 200 °C. Although this is well within the melting point of Inconel 625 (~1300 °C), we decided to paint the front tube white as a precautionary measure (Figure 51). Three different painting protocols were tested, and the solar reflectivity was measured for each.

Table 13. Paint reflectivity test results.

Coupon/Reflectometer Sample	Reflectivity (ρ_t)	Operations on Coupon
1	0.562±0.002	Painted (5 passes)
		Oxidized 24 hrs
2	0.540±.006	Oxidized 24 hrs
		Painted (5 passes)
		Cured
3	0.622±0.001	Painted (5 passes)
		Cured

Coupon 2 had the most stable surface following curing. Therefore, this process was used to paint the front tube. The solar reflectivity was measured to be 0.54 (solar absorptivity = 0.46).

Figure 51. Bladed receiver panels with front tube painted white with VHT Flame Proof Header Paint.

3.2.3.4 Receiver support structure and receivers in place for testing

The receiver required a support structure that could accommodate the two receiver designs to be tested. The support structure consists of 50.8 x 50.8 x 3.175 mm square tubing arranged in a rectangular fashion. The structure can hold the weight of the panels, the spillage board required for on-sun testing, and thermal insulation for all plumbing. This structure was arranged on two sliding rails to be able to move the structure back and forth in the test bay. The flexibility to move the structure in and out of the test bay allowed for access to the front of the receiver without requiring fall protection while working near the front of the solar tower. Figure 52 and Figure 53 show the SolidWorks CAD drawing and a back view of the as-built structure at the 220 test level of the Solar Tower.

During testing, the receivers will be exposed to high flux conditions (up to 200+ suns). Some of the flux present during the test will not be incident on the receiver, but on the surrounding features of the receiver. Additionally, components present on the tower for the test which lie in the movement path of the heliostat beams before and after testing need protection. These components are protected with spillage insulation boards. Duraboard HD is used for this

purpose around the receiver and in critical spots on the Solar Tower to protect the structure. It can resist lower flux levels for extended periods (greater than 1 hour seen on other DOE funded solar projects). When heated, the organic binders in the HD board burn out causing it to turn brown. After the burn out process, the board turns white again. Some of the pictures seen in this report will show brown HD board, but this is normal for using this board at high temperatures. Hardware (bolts, nuts, and washers) are protected from incident flux with round 76.2 mm diameter "pucks" made from this HD board.

The figures presented below are of the fabrication and testing of the receiver with more in-depth descriptions presented here. Figure 52 is a SolidWorks CAD model of the receiver structure with a representation of the bladed receiver in place. This structure was designed to hold the flat panel and bladed receiver as well as the ability to slide into and out of the test bay for ease of access. Figure 53 is an image of the back of the receiver structure with the flat panel receiver in place (no thermal insulation installed). Figure 54 is the water cooled panel that was utilized to obtain the incident power on the receivers. The center of the panel had a flux gauge installed to get a single point measurement needed for the calibration of the flux image taken on the front of the calibration panel during testing. Figure 55 shows the flat panel receiver in place in the structure before the tubes have been oxidized. This was a test fitting to ensure the structure provided enough clearance for the plumbing in the system. Figure 56 shows one flat panel receiver in place looking toward the heliostat field. You can see the back of the receiver panel as well as the inlet and outlet manifold ports for the air heat transfer fluid.

Figure 57 shows the flat panel receiver in place in the structure after the tubes have been oxidized. The oxidized tubes look blacker than the tubes seen in Figure 55. Figure 58 shows the final test structure for the flat panel receiver test. The spillage boards have been installed on the front of the receiver protecting the structure from incident flux. You can see some white between a few tubes at some points. This is the thermal insulation behind the receiver panels. The tubes did not align perfectly in the horizontal direction and there were a few small gaps on the order of 3mm in size. Figure 59 shows the flux gauge being installed in the water cooled panel. The flux gauge itself is water cooled to prevent failure. Figure 60 shows the thermal insulation installed behind the flat panel receiver. The insulation covered the inlet and outlet headers as well as the back of the receiver tubes to prevent heat loss from the system. You can see the instrumentation wires bundled down from the receiver.

Figure 61 shows the final test structure for the bladed panel receiver test. The spillage boards have been installed on the front of the receiver protecting the structure from incident flux. The spillage boards used for the flat panel receiver test were used if possible and you can see the brown color on these boards. Figure 62 shows the thermal insulation installed behind the flat panel receiver. The insulation covered the inlet and outlet headers as well as the back of the receiver tubes to prevent heat loss from the system. Any hose that had air going into a receiver panel was insulated. Due to the serpentine pattern of the heat transfer fluid in this receiver there was more insulation than the flat panel receiver. Figure 63 and Figure 64 show the receiver final setups after testing for the flat panel and bladed panel receivers, respectively. For comparison, Figure 65 shows the bladed receiver prior to insulation.
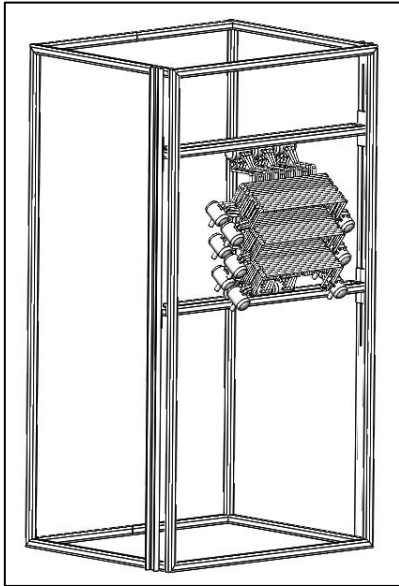
Figure 52. SolidWorks CAD drawing of receiver structure with bladed receiver panel in place

Figure 53. Back view of receiver support structure, as built at the 220 test level, back receiver panels can be seen in place

Flux gauge at center of panel
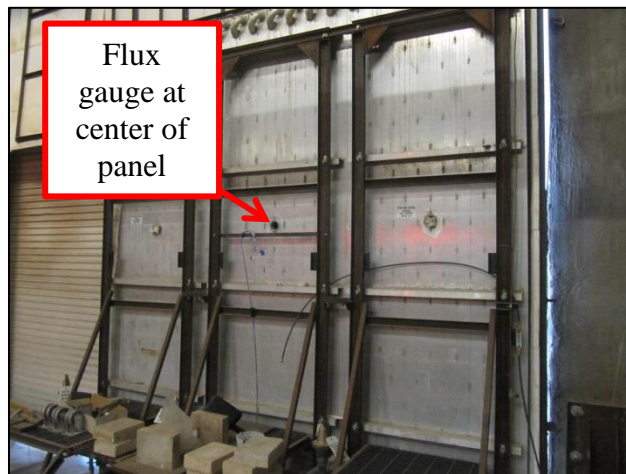
Figure 54. Water cooled flux panel used for incident power measurements during testing (back view)

Figure 55. Flat receiver panels in place before oxidation of the tubes

Figure 56. Back View of one back panel of tubes with the heliostat field in the background.
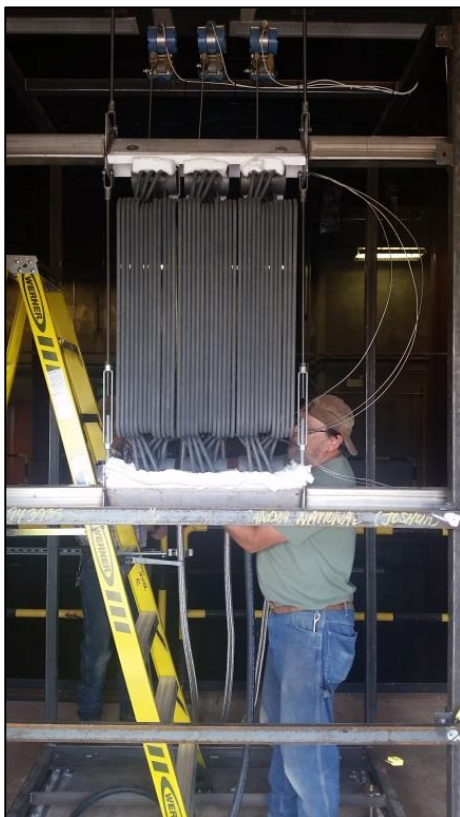
Figure 57. Flat receiver panels in place after oxidation

Figure 58. Spillage board installed for the flat panel receiver test

Figure 59. Flux gauge being installed in the water cooled panel of the test bay
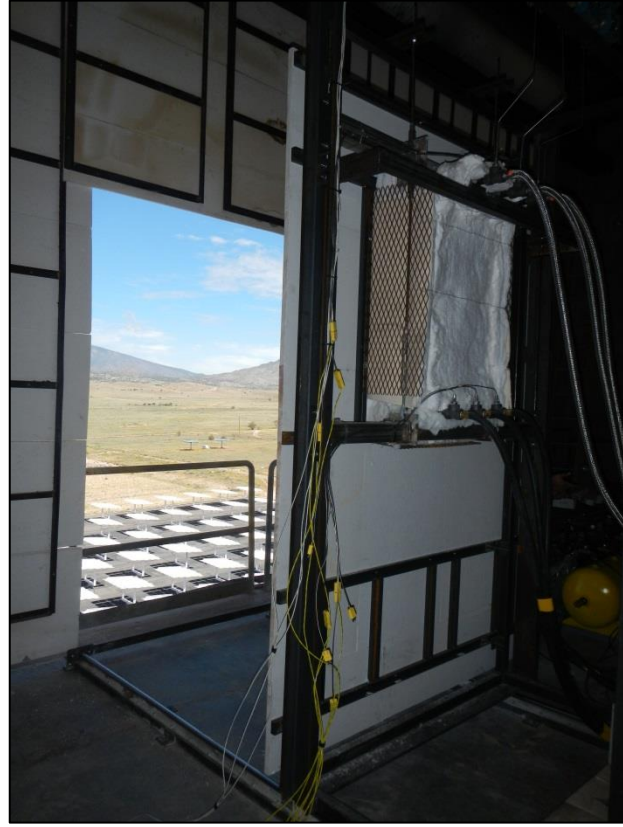
Figure 60. Thermal insulation in place for the flat panel receiver tests (view is behind the receiver at the plumbing)

Figure 61. Spillage board installed for the bladed receiver test

Figure 62. Thermal insulation in place for the bladed receiver tests (view is behind the receiver at the plumbing)

Figure 63. Flat panel receiver in place after on-sun testing

Figure 64. Bladed receiver in place after on-sun testing

Figure 65. Bladed receiver prior to final insulation.

3.2.3.5 Air supply

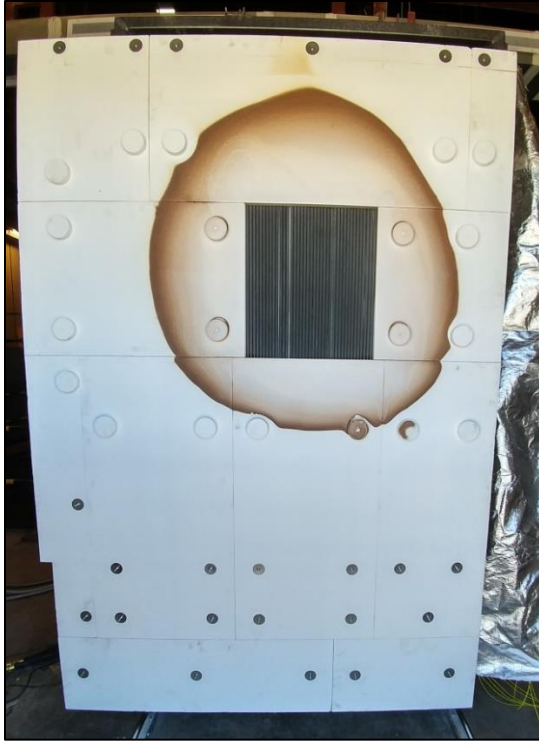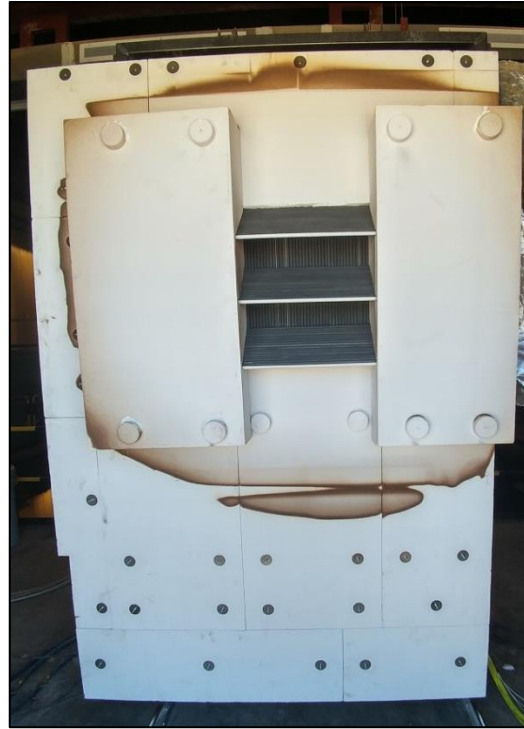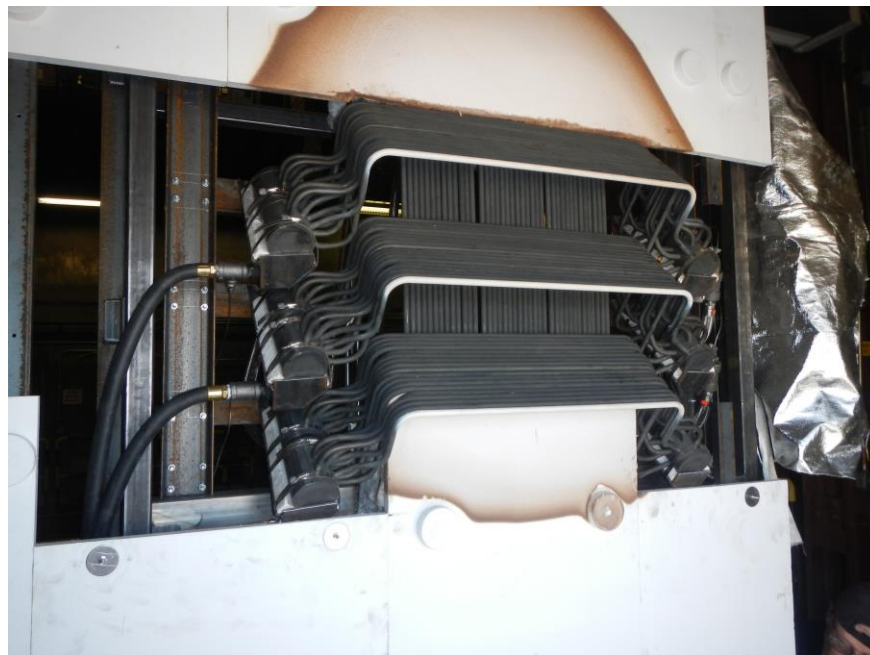The test required compressed air at 120 psi and up to 150 cfm (at the receiver) with associated sensors to measure temperature, mass flow rate, and pressure. To achieve this, an oil-free compressor (Atlas Copco ZT-55) was rented from Mesa Equipment. Oil-free compressed air was used to ensure that the receiver tubes could be used again with a different heat transfer medium without being contaminated by oil in the lines. A 1,000 gallon air receiver tank was used in-line after the compressor to reduce the load/unloading cycles needed to keep a relatively constant pressure in the system. During testing, the pressure band on the compressor was set to 5 psi which provided enough cycle time on the compressor. A single line was used to run the air up the tower to the 220 test level into a manifold that split the flow into three circuits that fed each flow loop in the two different receivers. The compressor provides 300 cfm and 125 psi at standard working conditions. The three circuits coming off the three-way manifold had individual instrumentation. Figure 66 shows the three-way manifold tank with the mass flow meters attached. The three circuits were controlled with ball valves which provided enough control to vary the flow rate into the receiver panels. Once the air leaves the receiver tank, it was diverted into an outlet exhaust pipe pre-existing in the Solar Tower. The exhaust was vented to the top of the tower to atmospheric conditions. A simple schematic of the overall system is seen in Figure 67. A more detailed setup is shown in Figure 68. Figure 69 shows the air compressor and 1000 gallon air receiver tank required for testing at the ground level of the Solar Tower.

Figure 66. Alicat mass flow rate sensors attached to the three outlet manifold tank
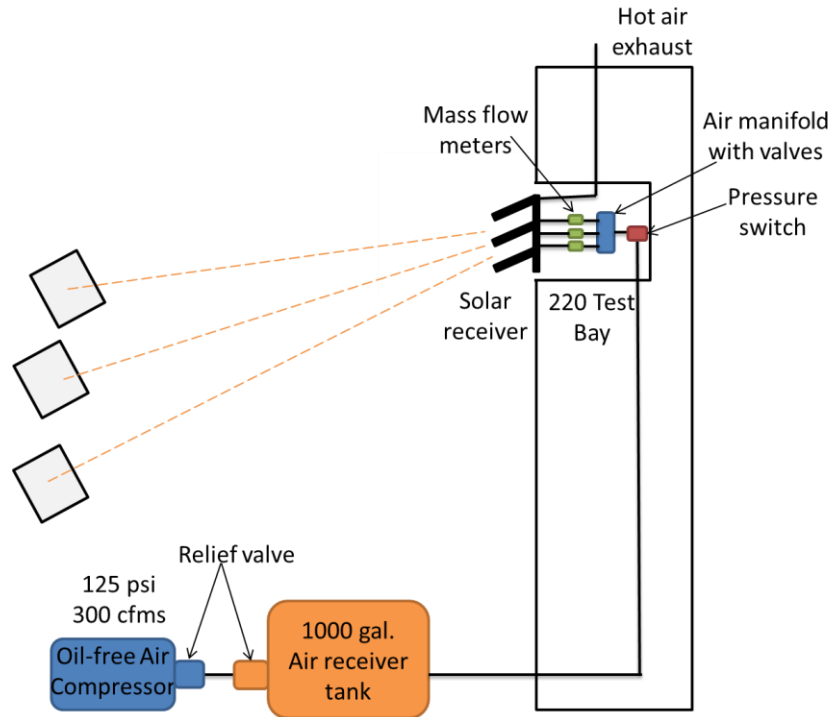
Figure 67. Simple schematic of the test configuration for the flat panel and bladed receiver tests
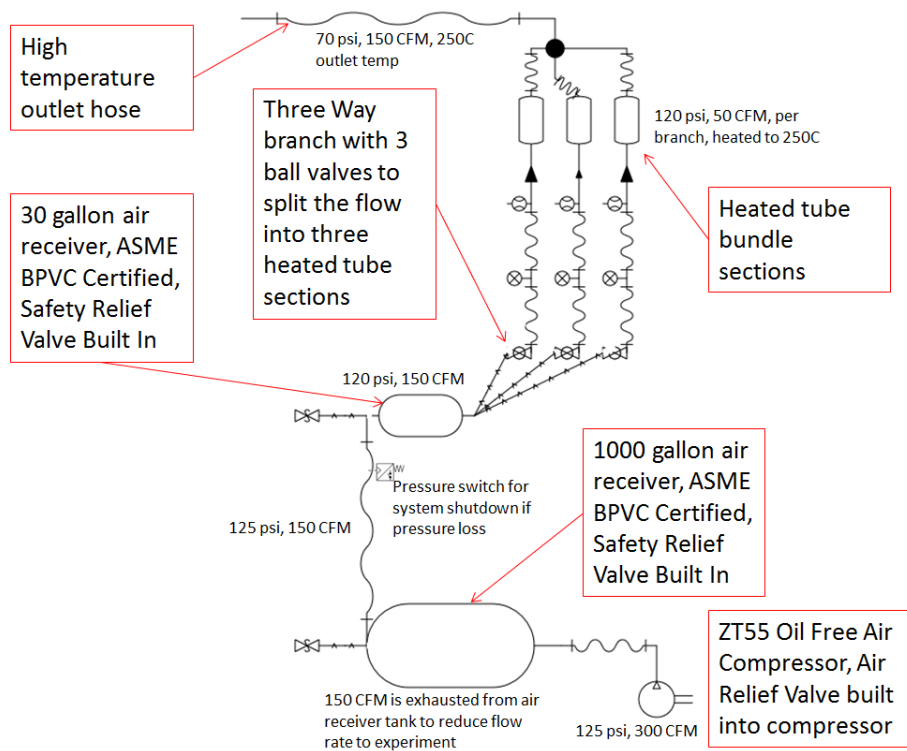

Figure 68. Detailed pressure system schematic for the test configuration

Figure 69. Air compressor (right in image) and 1000 gallon air receiver tank (yellow tank in image)

Each flow line had a temperature, mass flow rate, and pressure reading at the inlet. If there were transitions between panels (such as the bladed receiver) there were temperature measurements between these transitions.   Temperature and pressure were measured at the outlet of the receivers.   Type-K thermocouples were used for temperature measurement and were inserted into the flow through Swagelok t-joints that were rated well above the 827 kPa (120 psi) needed for the system. Mass flow rates and pressures at the inlet of the receiver were measured using Alicat M-1500SLPM-D sensors. The Alicat sensors read pressure up to 1103 kPa (160 psia) and mass flow rate up to 37 g/s. The three mass flow rate sensors can be seen in Figure 66 attached to the air tank manifold. The outlet pressures were measured using a Rosemount Model 1151GP pressure transmitter with a range from 0-2068 kPa (0-300 psi). The pressure transmitters were off-set from the flow by a stainless steel tube to prevent the transmitters from getting too hot which is seen in Figure 70. Figure 71 shows a photograph of on-sun testing of the bladed receiver design.
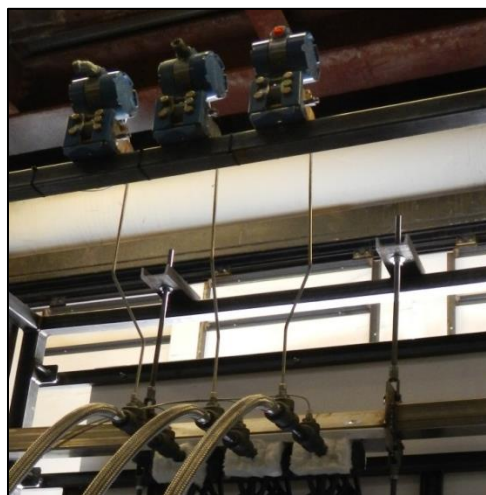
Figure 70. Three Rosemount pressure transmitters attached to the outlet receiver manifolds

Figure 71. On-sun testing of bladed receiver.

3.2.3.6 Test Results

The variation in all the temperatures recorded by the thermocouples was used to determine the steady-state regions where the relative uncertainty of the temperature increase was below 2% as shown in Figure 72. The temperature increase was recorded throughout all the tests. The average of the temperature and standard deviations were used to estimate the overall error propagation. The air temperature rise was 200 – 300 °C higher for the bladed receiver relative to the flat-panel receiver for the same average irradiance on the receiver tubes.
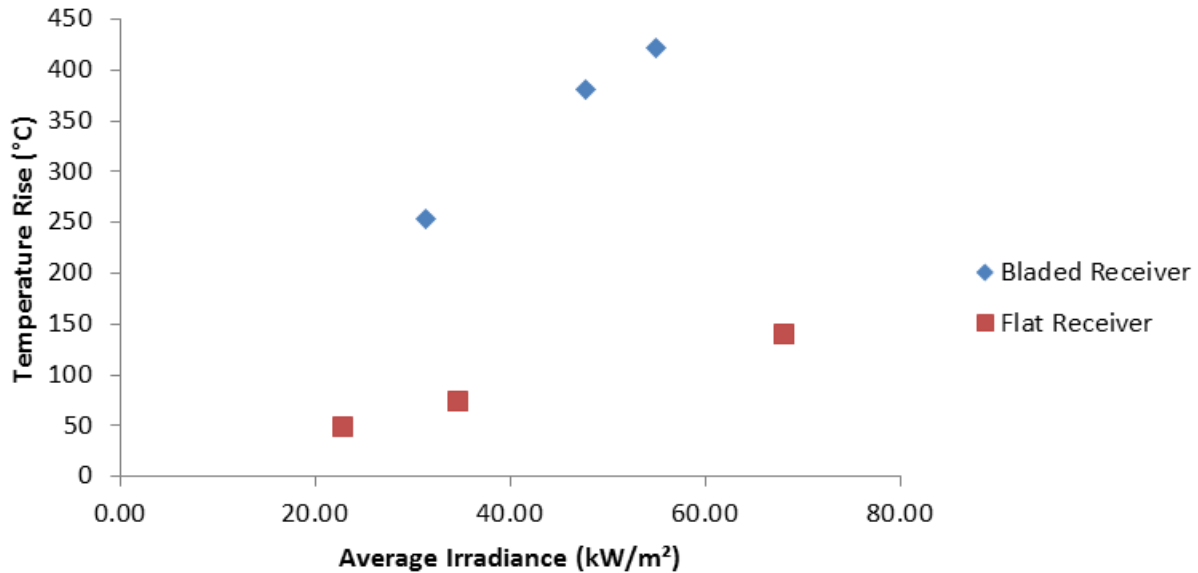
Figure 72. Air temperature increase recorded as a function of the incident flux recorded by the flux gauge. Error bars (not visible) correspond to one standard deviation.

The mass flow of air through the 3 sections of the receivers was recorded as well throughout the tests. The fluctuations in the mass flow rate observed in Figure 73 were caused by the load-unload cycle that the air compressor undergoes. The fluctuations have a consistent amplitude and frequency which is also another way to identify the steady-state region.
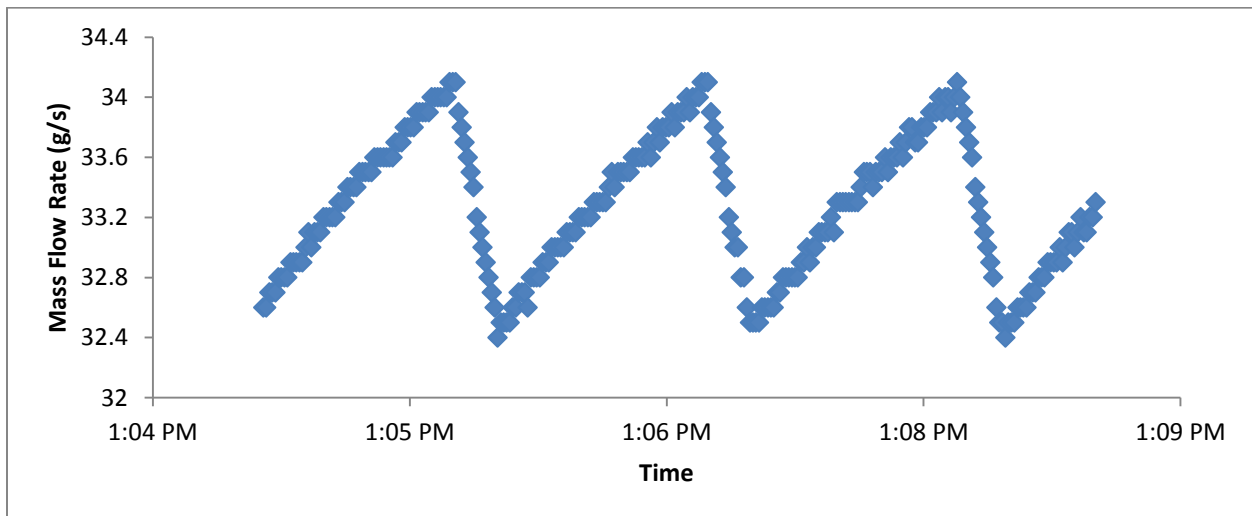
Figure 73. Mass flow rate fluctuations caused by the load-unload cycle of the air compressor.

Lastly, the impact on the heat flux centering was included to account for the error propagated in the measurements due to the misalignment of the beams. For every flux measurement, 4 more alternate positions were considered to produce a more conservative estimate of the power incident on the receivers. The images in Figure 74 illustrate the incident flux on the flux target was imposed in the receiver aperture.

74
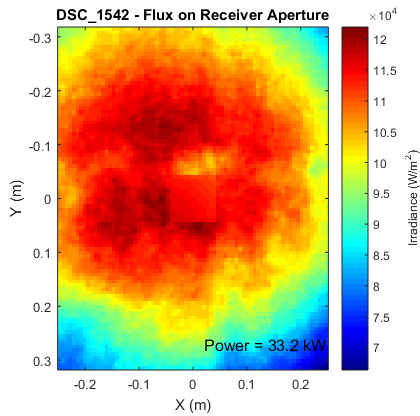
Beams centered about the flux gauge

Flux distribution using ray trace models
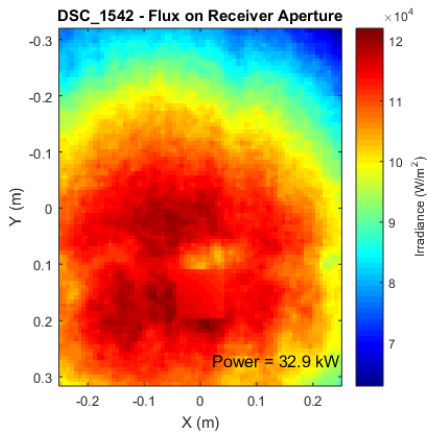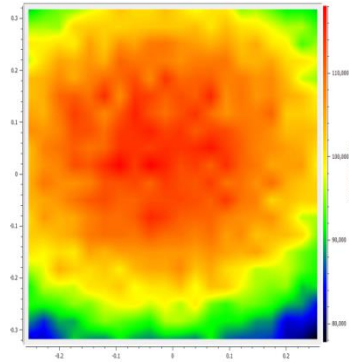
Shifting the beams 15 cm down
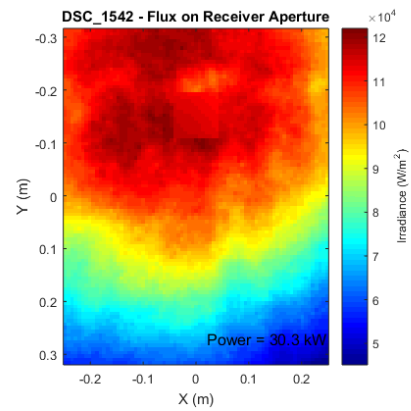
Shifting the beams 15 cm up
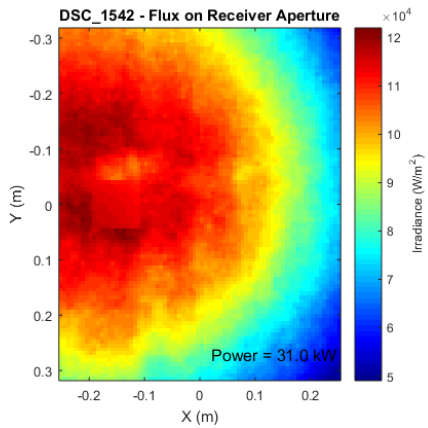
Shifting the beams 15 cm East
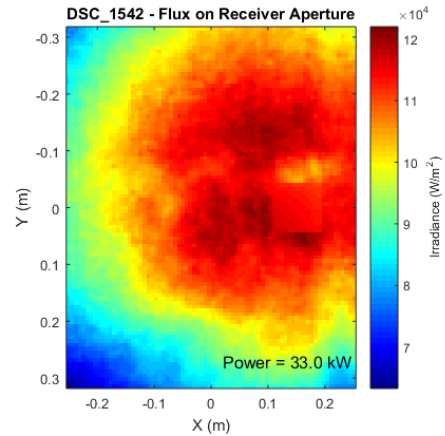
Shifting the beams 15 cm West

Figure 74. Flux distributions (11.85 W/cm2) imposed on the flat receiver aperture (0.635 m x 0.508 m) with alternate beam locations which represent the worst case scenario of a misalignment of the beams on the receiver. The centred flux matches the intensity and power on the aperture of the flux profile determined by ray trace. The patch in the center represents the locations of the flux gauge and the flux patch is generated by fitting the profile with a Lambertian distribution to match it.

In the example shown in Figure 74, outline of the receiver aperture (0.635 m x 0.508 m) was superimposed on the flux distribution (11.85 W/cm2) on the flux target. The aperture was was shifted 6" (0.15 m) in all directions (up, down, east, and west) t represent potential misalignment of the beams on the receiver. The case where the aperture is centered on the flux gauge is used to scale the flux profile determined by ray trace. The patch in the center represents the location of the flux gauge.

Since the flat receiver was coplanar with the aperture of the target board with the flux gauge, the power incident in that aperture was the same power incident on the receiver. On the other hand, for the bladed receiver the power incident on the aperture of the target board was different than the power incident on the receiver. Using ray tracing models, the incident power in the receiver could be determined. Initially the power on the target board aperture and a virtual aperture that is coplanar are matched. The virtual aperture is then removed and the incident power can be calculated on the receiver tubes as seen in Figure 75. The incident power on the receiver tubes was used to calculate the thermal efficiency of the receiver.
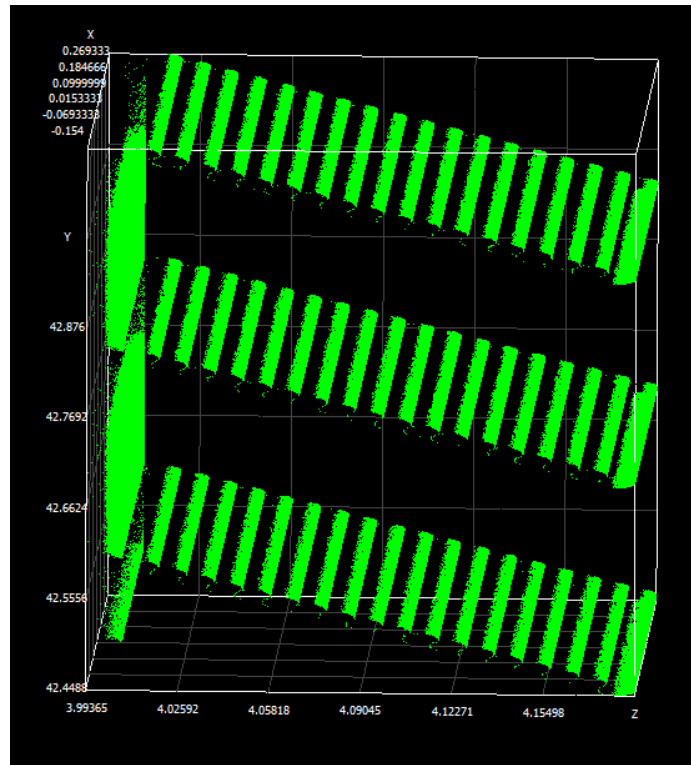

Figure 75. Ray intersections computed on the receiver surface using ray tracing modelling.

The thermal efficiencies as a function of the irradiance incident on each receiver was calculated as follows:

$$Thermal\ Efficiecncy = \frac{\sum \dot{m} \int_{Tin}^{Tout} C_p(T)dT}{\dot{Q}_{incident}}$$

where $\dot{m}$ is the total mass flow rate of air per section, Tin and $Tout$ are the Inlet and outlet air temperatures, $C_p(T)$ is the heat capacity of air and $\dot{Q}_{incident}$ is the total power incident on the receiver. Figure 76 shows the thermal efficiencies as a function of the average irradiance on the receiver tubes. Results show that for a given average irradiance, the bladed receiver yields a thermal efficiency that is ~5 percentage points higher than the flat receiver. The thermal efficiency decreased with increasing irradiance because at a fixed air mass flow rate, the tube temperature increased with increasing irradiance, yielding larger radiative and convective heat losses.
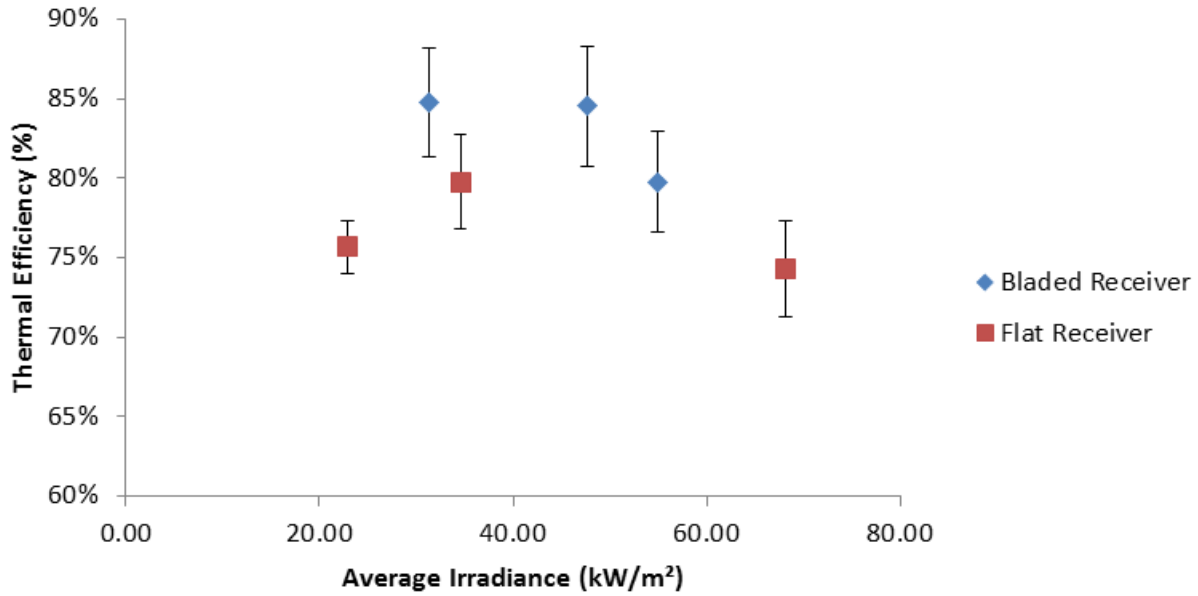
Figure 76. Thermal efficiency recorded as a function of the incident flux recorded by the flux gauge. The error bars correspond to the standard deviation from the mean.

4   CONCLUSIONS

Fractal-like receiver designs with novel light-trapping geometries and features at multiple length scales have been developed and tested. At the macro scale, bladed panel configurations were simulated and shown to reduce radiative heat losses and increase thermal efficiencies by increasing the effective solar absorptance and reducing heat losses. At the meso scale, novel tubular geometries were modeled and tested to evaluate their impacts on the effective solar absorptance and thermal efficiency. Modeling results showed that the corrugated structures could increase the effective solar absorptance by several percentage points at intrinsic material solar absorptances of ~85%, and the impact was greater when the intrinsic material solar absorptance was lower. At high material intrinsic solar absorptances (95% or greater), the enhancement was negligible. The thermal efficiency could also be increased by several percentage points depending on the intrinsic solar absorptance. Preliminary structural analyses

showed that high stresses near corners could exceed the maximum allowable stress for certain working fluids and operational conditions. Rounded corners and thicker tubes could alleviate the problem.

Tests were performed using meso-scale prototypes fabricated from Inconel 718 using powder-bed fusion additive manufacturing techniques. The parts were exposed to 30 W/cm^2 in a solar furnace and reached temperatures of ~700 °C. Measurements of the irradiance distribution and comparisons with ray-tracing models showed that the effective solar absorptance was increased in parts with corrugations and fins and corroborated the modeling results.

Results indicate that the use of fractal-like geometries and features at both the meso and macro scales can increase the effective solar absorptance of oxidized substrates (e.g., Haynes 230, Inconel 718) from ~90% to greater than 95% without the need for coatings or high-temperature paints, which can degrade over time.

Calorimetric tests of the meso-scale parts showed that the fractal-like geometries yielded higher thermal efficiencies in all of the designs. The results showed that relative to a flat plate (base case), the new FLGs exhibited an increase in the effective solar absorptance from 0.86 to 0.92 for an intrinsic material absorptance of 0.86. Peak surface temperatures of ~1000°C and maximum air temperature increases of ~200°C were observed. Compared to the base case, the new FLGs showed a clear air outlet temperature increase. Thermal efficiency increases of ~15%, with respect to the base case, were observed. These devices were fabricated using powder-bed fusion, an additive manufacturing technique, to create the complex geometries and features from Inconel 718, a high-temperature nickel alloy. This unique method may one day be used to fabricate entire sections of solar receivers.

Macro-scale tests were conducted using flat and horizontal bladed receiver designs. Pressurized air was used as the heat-transfer fluid. The irradiance on the tubular receiver panels was prescribed to yield similar average irradiance values for the two sets of tests, which ranged from ~20 – 70 kW/m^2. The peak flux on the aperture of the bladed receiver panel (over 200 kW/m^2) was significantly higher than the peak flux on the flat panel (~80 kW/m^2), which is one of the advantages of the fractal-like designs – the ability to accommodate higher concentration ratios with smaller optical apertures. Results showed that the air temperature rise in the bladed receiver panel was 200 – 300 °C higher than in the flat panel, and the thermal efficiencies were ~5 percentage points higher.

REFERENCES

[1] Ho, C.K., A.R. Mahoney, A. Ambrosini, M. Bencomo, A. Hall, and T.N. Lambert, 2014, Characterization of Pyromark 2500 Paint for High-Temperature Solar Receivers, *Journal of Solar Energy Engineering-Transactions of the Asme*, **136**(1).

[2] Garbrecht, O., F. Al-Sibai, R. Kneer, and K. Wieghardt, 2013, CFD-simulation of a new receiver design for a molten salt solar power tower, *Solar Energy*, (90), p. 94-106.

[3]   Kasperski, J. and M. Nems, 2013, Investigation of thermo-hydraulic performance of concentrated solar air-heater with internal multiple-fin array, *Applied Thermal Engineering*, (58), p. 411-419.

[4]   Wagner, M., 2015, Direct s-CO2 Receiver Development (Quad Chart), NREL,

[5]   Ho, C.K., J.M. Christian, and J. Pye, United States Patent Application 61/901628, Solar Thermal Advanced Receiver for Concentrating Solar Power Towers, S. Corporation, November 8, 2013.

[6]   C.K. Ho et al., United States Patent Application 62/015052, Fractal Materials and Designs with Optimized Radiative Properties, Sandia Corporation, June 20, 2014.

[7]   Yellowhair, J., J.M. Christian, and C.K. Ho, 2014, *Evaluation of Solar Optical Modeling Tools for Modeling Complex Receiver Geometries*, in *Proceedings of the ASME 2014 8th International Conference on Energy Sustainability*, Boston, MA, June 29 - July 2.

[8]   National Renewable Energy Laboratory. *SolTrace Optical Modeling Software*. Available from: http://www.nrel.gov/csp/soltrace/.

[9]   Yellowhair, J.E., C.K. Ho, J.D. Ortega, J.M. Christian, and C.E. Andraka, 2015, *Testing and Optical Modeling of Novel Concentrating Solar Receiver Geometries to Increase Light Trapping and Effective Solar Absorptance*, in *Proceedings of the SPIE Optics+Photonics Solar Energy+Technology High and Low Concentrator Systems for Solar Energy Applications X*, San Diego, August 9 - 13, 2015.

[10] Ho, C.K., J.M. Christian, J.D. Ortega, J. Yellowhair, M.J. Mosquera, and C.E. Andraka, 2014, *Reduction of radiative heat losses for solar thermal receivers*, in *Proceedings of the SPIE Optics+Photonics Solar Energy+Technology High and Low Concentrator Systems for Solar Energy Applications IX*, San Diego, August 17 - 21, 2014.

[11] Ortega, J.D., J.M. Christian, and C.K. Ho, 2015, *Coupled Optical-Thermal-Fluid and Structural Analyses of Novel Light-Trapping Tubular Panels for Concentrating Solar Power Receivers*, in *Proceedings of the SPIE Optics+Photonics Solar Energy+Technology High and Low Concentrator Systems for Solar Energy Applications X*, San Diego, August 9 - 13, 2015.

[12] Ortega, J., S. Khivsara, J. Christian, C. Ho, and P. Dutta, 2016, Coupled modeling of a directly heated tubular solar receiver for supercritical carbon dioxide Brayton cycle: Structural and creep-fatigue evaluation, *Applied Thermal Engineering*, (http://dx.doi.org/10.1016/j.applthermaleng.2016.06.031).

[13] Ortega, J., S. Khivsara, J. Christian, C. Ho, and J. Yellowhair, 2016, Coupled modeling of a directly heated tubular solar receiver for supercritical carbon dioxide Brayton cycle: Optical and thermal-fluid evaluation, *Applied Thermal Engineering*, (http://dx.doi.org/10.1016/j.applthermaleng.2016.05.178).

[14] Christian, J. and C. Ho, 2012, *CFD Simulation and Heat Loss Analysis of the Solar Two Power Tower Receiver*, in *ASME 2012 Energy Sustainability and Fuel Cell Conference*, San Diego, CA, July 23-26.

[15] Ho, C., J. Christian, J. Ortega, J. Yellowhair, M. Mosquera, and C. Andraka, 2014, *Reduction of radiative heat losses for solar thermal receivers*, in *SPIE Optics and Photonics for Sustainable Energy*, San Diego, CA,

[16] United States Patent U.S. Patent Application 14535100, Filed Nov. 6, 2014, BLADED SOLAR THERMAL RECEIVERS FOR CONCENTRATING SOLAR POWER,

[17] Christian, J., J. Ortega, and C. Ho, 2015, *Novel tubular receiver panel configurations for increased efficiency of high-temperature solar receivers*, in *ASME International Conference on Energy Sustainability*, San Diego, California,

[18] Christian, J.M., J.D. Ortega, and C.K. Ho, 2015, *Novel Tubular Receiver Panel Configurations for Increased Efficiency of High-Temperature Solar Receivers*, in *ASME Proceedings of the 9th International Conference on Energy Sustainability*, San Diego, CA, June 28 - July 2, 2015.

[19] Ho, C., A.R. Mahoney, A. Ambrosini, M. Bencomo, A. Hall, and T. Lambert, 2012, *Characterization of Pyromark 2500 for High-Temperature Solar Receivers*, in *International Conference on Energy Sustainability*, San Diego, CA,

[20] Ortega, J., J. Christian, and C. Ho, 2015, *Structural Analysis of a Direct Heated Tubular Solar Receiver for Supercritical CO2 Brayton Cycle*, in *ASME Energy Sustainability* San Diego, California,

[21] Ho, C.K., J.M. Christian, J. Pye, and J.D. Ortega, United States Patent Application SD12644.1/S132227, Solar Thermal Receivers with Multi-Scale Light Trapping Geometry and Features, Sandia Corporation, June 19, 2015.

[22] Ho, C.K. and S.S. Khalsa, 2012, A Photographic Flux Mapping Method for Concentrating Solar Collectors and Receivers, *Journal of Solar Energy Engineering-Transactions of the Asme*, **134**(4).

DISTRIBUTION

Sandia (all electronic copies):

| 1 | MS-0899 | Technical Library | 9536 |
| 1 | MS0359 | D. Chavez, LDRD Office | 1911 |